ORIGINAL ARTICLE

Effect of pre-cut hole diameter on deformation mechanics in multi-stage incremental hole flanging of deep drawing quality steel

Praveen Kumar Gandla[1] · Suresh Kurra[1] · K. Sajun Prasad[2] · Sushanta Kumar Panda[2] · Swadesh Kumar Singh[3]

Abstract

Incremental hole flanging (IHF) is a relatively new sheet metal forming process to produce intricate shapes without using dedicated punches and dies. The present work focuses on understanding the mechanics of the multi-stage IHF process through experimental studies and the finite element approach. The IHF experiments were performed on deep drawing quality steel sheets with a pre-cut hole diameter of 45 mm, 50 mm, 60 mm, and 70 mm. The cylindrical flanges were formed in four stages with an initial wall angle of 60° to a final angle 90° with an angle increment of 10° in each stage. The maximum and minimum hole expansion ratio was found to be 2.06 and 1.17 respectively. The fracture was observed in a blank of 45 mm pre-cut hole diameter in the third stage at 40 mm depth. The fracture forming limit diagram (FFLD) was determined from incrementally formed varying wall angle conical and pyramidal frustums. Consequently, six different ductile damage models incorporating Hill48 anisotropy plastic theory were successfully calibrated. The Ayyada model showed good agreement with experimental FFLD as compared to all other models. The fracture limit determined experimentally and using the Ayyada model was implemented in the finite element simulation of the IHF process to predict the formability in terms of in-plane strain distribution, forming forces, and thickness distribution. The predicted results matched accurately with the experimental data within a 6% error for all investigated conditions. Noticeably, the strain path in IHF had three deformation modes viz. plane strain, bi-axial stretching, and uni-axial tension, which was comprehended using texture analyses. Finally, irrespective of the initial pre-cut hole diameter, the surface roughness was found to decrease with the number of stages of the IHF process.

Keywords Incremental hole flanging · Strain distribution · Limiting forming ratio · Finite element simulations · Forming forces · Surface roughness · Ductile fracture models

1 Introduction

Flanging is a process of bending the sheet edges to impart a smooth rounded edge with high strength and rigidity. Flanging can be divided into several sub-operations, such as shrink flanging, stretch flanging, hole flanging, and tube flanging [1]. Amongst them, the Conventional Hole Flanging (CHF) process is widely adopted in several automobile and aerospace applications [2]. In this process, a blank with a pre-cut hole is plastically deformed by a conical or dome-shaped punch to produce short vertical or conical flanges, subsequently assembled with the mainframe components. In hole flanging, the magnitude of material deformation is expressed by Hole Expansion Ratio (HER). The HER measures the amount of deformation in the flanged part as a function of inner diameter of a finished flange (d_f) and initial pre-cut hole diameter (d_i) as given by Eq. 1.

$$\text{HER} = \frac{d_f}{d_i}. \tag{1}$$

The formability of the material in CHF is generally quantified using Limiting Forming Ratio (LFR). The LFR measures the formability of material corresponds to maximum HER without failure. It is a ratio of the maximum inner diameter of the finished flange and minimum pre-cut hole diameter in the blank as shown in Eq. 2.

✉ Suresh Kurra
   ksuresh@hyderabad.bits-pilani.ac.in

1   Department of Mechanical Engineering, BITS Pilani, Hyderabad Campus, Hyderabad 500078, India

2   Department of Mechanical Engineering, I.I.T. Kharagpur, Kharagpur, West Bengal 721302, India

3   Department of Mechanical Engineering, GRIET, Hyderabad 500072, India

$$\text{LFR} = \text{HER}_{\max} = \frac{(d_f)_{\max}}{(d_i)_{\min}}. \qquad (2)$$

Apart from cylindrical and conical flanges, the hole flanging process can also be used to produce square and elliptical shaped flanges using proper punches and dies during forming [3, 4]. The LFR of elliptical flanges is defined as the ratio of punch circumference to minimum elliptical pre-cut hole circumference drawn by punch without any fracture. The maximum thinning occurs at the end of the major axis of the expanded hole. The punch load variation with punch stroke was in a bell-shaped curve reminiscent of the typical IHF process and predicted results showed a similar trend as reported in [3].

Numerous studies have reported the combined effect of process parameters, deformation modes, and failure in the CHF process. The research investigations proved that some of the crucial variables such as initial yield stress, strain-hardening, plastic anisotropy, sheet thickness, edge quality of pre-cut hole, lubrication condition, the punch shapes, blank holding force, and the clearance between tool affect the process mechanics in CHF [5–9]. The influence of punch semi-cone angle on flange shape, formability, thickness distribution, and punch load was studied on steel sheets by varying the angle within the range of 15°–90° [5]. The study demonstrated that the cone semi-angles had a significant effect on flange shape. Large cone angles produce spring back, whereas spring forward occurs at smaller cone semi-angles. The LFR is independent of the semi-cone angle of punch. However, the maximum punch force increases remarkably with a semi-cone angle. Also, the maximum force decreases linearly with an increase in the diameter of pre-cut hole. Additionally, the wall thickness decreases linearly with depth and found that the thickness at the fracture in hole flanging is equal to the fracture thickness under a simple tension test. The effect of punch shape was studied with four different punch shapes viz. spherical, ellipsoid, flat, and conical frustum punch head in CHF through finite element simulations [8]. The results showed that the strain path is independent of punch shape, but the maximum punch load depends on punch shape. The punch load is minimum with the ellipsoidal punch and maximum with the flat punch. A similar study was conducted on DDQ steels with conical, spherical, and cylindrical punches and found that the punch shape affects the hole expansion limit [10]. The largest hole expansion was achieved when flanging with the conical punch and the worst in the case of the cylindrical (flat-bottomed) punch. Also, HER increased with the strain hardening exponent and plastic anisotropy irrespective of the punch geometry.

The effect of edge quality of pre-cut hole using Conventional Punching (CP) and Fine Blanking (FB) process was studied through experiments and numerical simulations [6]. The FE simulation of these two blanking processes was carried out in DEFORM software implementing Ayyada fracture model. The simulations revealed that the maximum damage value in the CP process than FB processed hole. Due to this, the crack propagation was started at the middle stage of CP hole flanging, reducing the effective flange height. Whereas no cracks were formed on the flange lip in the FB flanging process resulted in improved flange height. The hole flanging studies were also performed on high-strength steel sheets such as TRIP steels and ferrite–bainite steels to investigate the formability, fracture, and lip shape behaviors [7]. Researchers also have demonstrated the hole flanging operation using fixed blank-holder, without blank-holder, constant blank-holding force, and with progressive blank-holding force [9]. The result revealed that the blank-holding condition does not affect the maximum punch load; however, it has an essential effect on the kinematics of the outer edge of the workpiece that ultimately affects the shape of the finished product.

In CHF, the fracture occurs at the hole periphery due to circumferential tensile stresses. Therefore, fracture thickness strain obtained from a simple tensile test is used to predict the fracture in CHF [11]. Some researchers used different ductile damage models such as Oyane's, Cockroft and Latham, Lemaitre and Gurson–Tvergaard–Needleman (GTN) to predict the fracture in the hole expansion process [12–14]. The constants in Oyane's ductile damage model are estimated from the fracture strains obtained from simple uniaxial tensile and plane-strain tests [12]. The developed Oyane model showed suitability in predicting the fracture initiation and the critical stroke in hole expansion of mild steel and high strength steel blanks with 10 mm diameter pre-cut hole. Cockroft and Latham, Oyane, and Lemaitre ductile damage models were also successfully used to predict the fracture in hole flanging of oil filter cover [13]. At the failure moment, the local strain distributions between different phases were studied, and correlated with macroscopic deformability results.

Many studies on hole flanging proved that the fracture limit depends on material properties such as plastic strain ratio (r_m), strain hardening exponent (n) and total transverse elongation (e_t) [15, 16]. The researchers proposed various empirical relations as a function of these parameters to evaluate HER of different materials. For machined holes in HSLA steel sheets, the HER was expressed as a function of r_m and e_t [16]. This equation was further modified by including other steel grades such as nineteen ferritic, ferritic stainless, and austenitic stainless steels [15]. The empirical equations for sheared-hole expansion tests were developed as a function of r_m and n. The inhomogeneous deformation behavior in oblique flanges was studied through electromagnetic forming experiments and simulations [17]. The area

of deformation region, the electromagnetic force and die constraints were found to be the main influencing factors on inhomogeneous deformation.

The CHF requires dedicated tooling and is suitable for mass production. The recently developed Incremental Sheet Forming (ISF) process is gaining more attention due to its die less nature and simple tooling. There are numerous studies on ISF to understand the strain distribution, failure modes, formability, form accuracy, tool path optimization [18–20]. The accurate prediction of forming forces is vital to estimate the tool deflection and springback. These parameters are used further for tool path compensation for improving the geometric accuracy of formed components [19]. The form accuracy of the ISF parts was proved to be enhanced by closed-loop control of the tool path [20]. The proposed methodology has been validated by incrementally forming the funnel, bowl, and two-section cone geometries. Apart from modifying the tool path, researchers proposed alternative strategies such as partial/full rigid dies, flexible dies made of foams, providing the slave tool for local support, and providing the peripheral support to improve the accuracy of the formed part [22]. The effect of all these strategies and their combinations were studied through experiments and finite element simulations by forming an L-shape component. Further, the formability of aluminum material in the ISF process was evaluated using experimental FLDs, and the failure modes of the material were correlated with microstructural studies [21].

In ISF process, the required shape of the part can be obtained by deforming the material in a single stage or multiple stages at room temperature as well as elevated temperatures, and the process can be adopted for producing macro components as well as micro components. There are different variants of ISF processes such as Two Point Incremental Forming (TPIF), Incremental Hole Flanging (IHF) and Incremental Tube Forming (ITF) [21, 22]. The IHF process has proven to be a good alternative for CHF to produce different shapes of the flanges with simple tooling. In the IHF process, a blank with pre-cut hole is rigidly fixed by a blank holder around its outer periphery. The blank is then progressively deformed by CNC controlled hemispherically headed tool to produce smooth flanges. Most of the IHF studies focused on evaluating stress–strain distribution, thickness distribution, fracture prediction, and understanding the effect of process parameters on formability. The strain mapping was appraised using circle grid analysis and extended to stress space by combining the plasticity relations [23]. The failure limit of the material was accessed using different ductile damage models such as Cockcroft and Latham, Ayada and Rice-Tracey. The critical damage parameters were evaluated from the maximum effective strain at the onset of failure. The results concluded that the failure occurs in the flange wall due to meridional stresses acting under plane strain loading conditions [24].

Some researchers have proposed different tool path strategies to achieve uniform thickness distribution during IHF processes [25]. Also, the introduction of flanging tool geometry similar to ball nose milling cutter showed to improve the thickness distribution and forming limits during the IHF process [26]. The performance of the flange tool was validated using analytical and finite element models. In this context, the effect of various process parameters such as tool diameter, pre-cut hole diameter, and spindle speed were analyzed during single-stage IHF of AA7075-O aluminum alloy sheet of 1.6 mm thickness. Unlike uniaxial tension failure at the hole edges in the CHF process, the sheet was found to be failed around the mid-way of the flange region due to bi-axial stretching [27].

Based on the above discussion, the literature review reveals that the CHF process is well-established. However, there are minimal studies on the IHF process, and it is still at the nascent stage. Moreover, the LFR used in the CHF process does not provide enough information on the deformation mechanism, fracture location, thickness distribution, and type of failure. Therefore, the present paper aims to understand the process mechanics of the multi-stage IHF process. The strain distribution of DDQ steel sheets in multi-stage IHF with different pre-cut hole diameters are analyzed using experimental and theoretical fracture limit. Further, the effect of pre-cut hole diameter and number of forming stages on forming forces, thickness distribution, and surface roughness are analyzed using experiments and finite element simulations.

2 Materials and methods

2.1 Mechanical characterization

A batch of 1 mm thick rolled DDQ steel sheets were used in this study. The uniaxial tensile tests were performed using Zwick/Roell universal testing machine at a deformation speed of 0.3 mm/min to obtain the mechanical properties. The sheets were cut in three different orientations i.e., rolling (0°), diagonal (45°), and transverse (90°) to the rolling direction of the sheet. The tensile samples were fabricated as per the ASTM standard E8/E8M-09 specifications [28, 29]. The mechanical properties such as yield strength (YS), ultimate tensile strength (UTS), anisotropy coefficient (r), and elongation at break are presented in Table 1. The average value of the anisotropy coefficient $\bar{r}$ was obtained from Eq. 3. The mechanical properties in different orientations of the sheet are as given in Table 1.

$$\bar{r} = \frac{r_0 + 2r_{45} + r_{90}}{4}. \tag{3}$$

The stress–strain curve obtained from the tensile test was approximated by Holloman's hardening law as shown in Eq. 4.

Table 1 Mechanical properties of the DDQ steel sheets of 1 mm thickness

Material	Sheet orientation	YS (MPa)	UTS (MPa)	% elongation	r value	$\bar{r}$
DDQ steel	0°	204	320.7	30.9	1.22	1.18
	45°	206	330.2	30.9	1.21	
	90°	208	328	30.3	1.08	
Average (P)		206	327.2	30.75		

$P = 0.25(P_0 + 2P_{45} + P_{90})$, where P = YS, UTS, % elongation $\bar{r} = 0.25(r_0 + 2r_{45} + r_{90})$

$$\sigma = 519\varepsilon^{0.176} \tag{4}$$

2.2 Multi-stage incremental hole flanging experiments

As-rolled DDQ steel sheets were cut to the required dimension of 250 mm × 250 mm for multi-stage IHF experiments. The experiments were carried out on a 3 axis Hardinge Bridgeport CNC milling machine. The schematic diagram of the IHF process and its corresponding experimental setup are shown in Fig. 1. The setup consists of a fixture to hold the blank with a blank holder and a backing plate with a 110 mm diameter hole. The blanks were cut with a central hole of 45 mm, 50 mm, 60 mm, and 70 mm diameter to study its effect on formability. The blanks were electrochemically etched with circular grids of 3 mm diameter to measure the in-plane principal strains after forming. The major and minor axis of the deformed grid was measured using a stereo zoom microscope and image analyzer software. Further, the major and minor principal strains were evaluated using the following equations.

$$\varepsilon_1 = \ln\left(\frac{L_{\text{major}}}{d_0}\right), \tag{5}$$

$$\varepsilon_2 = \ln\left(\frac{L_{\text{minor}}}{d_0}\right), \tag{6}$$

where ε_1 and ε_2 represents the major and minor true strains. L_{major}, L_{minor} and d_0 denote the length of the major axis length of the deformed grid, minor axis length of the deformed grid, and initial grid diameter, respectively.

The vertical flanges were formed by incrementally deforming the blank in four stages with an initial drawing angle of 60° in an increment of 10°. The experimental plan for the multi-stage IHF process is consolidated in Table 2. The spiral tool path for each stage was generated using MASTER CAM software. The blanks were formed with a 10 mm diameter hemispherical headed tool made of EN26 steel heat-treated to 60 HRC. All the experiments were conducted with grease as a lubricating agent at a spindle speed and step depth of 250 rpm and 0.5 mm, respectively. The

forming forces during IHF operation were measured using a strain-gauge type dynamometer placed between the machine tool bed and forming fixture, as shown in Fig. 1b. The forces were acquired in x–y–z directions with a sampling rate of 10,000 s^{-1}. Finally, the formed parts were cut using wire-cut EDM, and the wall thickness was measured using a pointed anvil micrometer with the least count of 0.01 mm. Besides, the surface roughness of formed parts after each stage was measured using Taylor Hubson Talysurf.

2.3 Finite element analysis

The finite element (FE) simulations of the multi-stage IHF process were carried out using LS-Dyna software. The blank was modeled with shell elements with a central hole of 45 mm, 50 mm, 60 mm, and 70 mm. Figure 2 shows the FE model of tools such as a blank, forming tool, blank holder, and backing plate. All tools were modeled using shell elements and treated as rigid bodies (MAT 20). The blank material was modeled as deformable elastoplastic material with a power-law hardening model (MAT 18). The material properties of the blank are incorporated as per Table 1. The contact between the tool and blank was modeled using the One_Way_Surface_to_Surface algorithm [30], and the friction between tool and blank was considered using Coulomb friction law with a coefficient of friction 0.01 [31]. The edges of the blank were fixed to prevent the drawing of material during deformation. The motion of the forming tool is controlled in the simulations by inputting the tool path trajectories generated using Master CAM software in the form of time position data, as shown in Fig. 3. The long computational time associated with longer tool paths were minimized by using mass scaling and time scaling techniques [32].

2.4 Microtexture and surface roughness

Microtexture analyses at different strain levels of successfully formed multi-stage IHF components were done to correlate the mechanical responses with the metallurgical aspects. The multi-stage IHF with an initial hole diameter of 60 mm is considered to comprehend the change in the strain path within the deformed sample and with a change in increment angle. The samples from different locations of
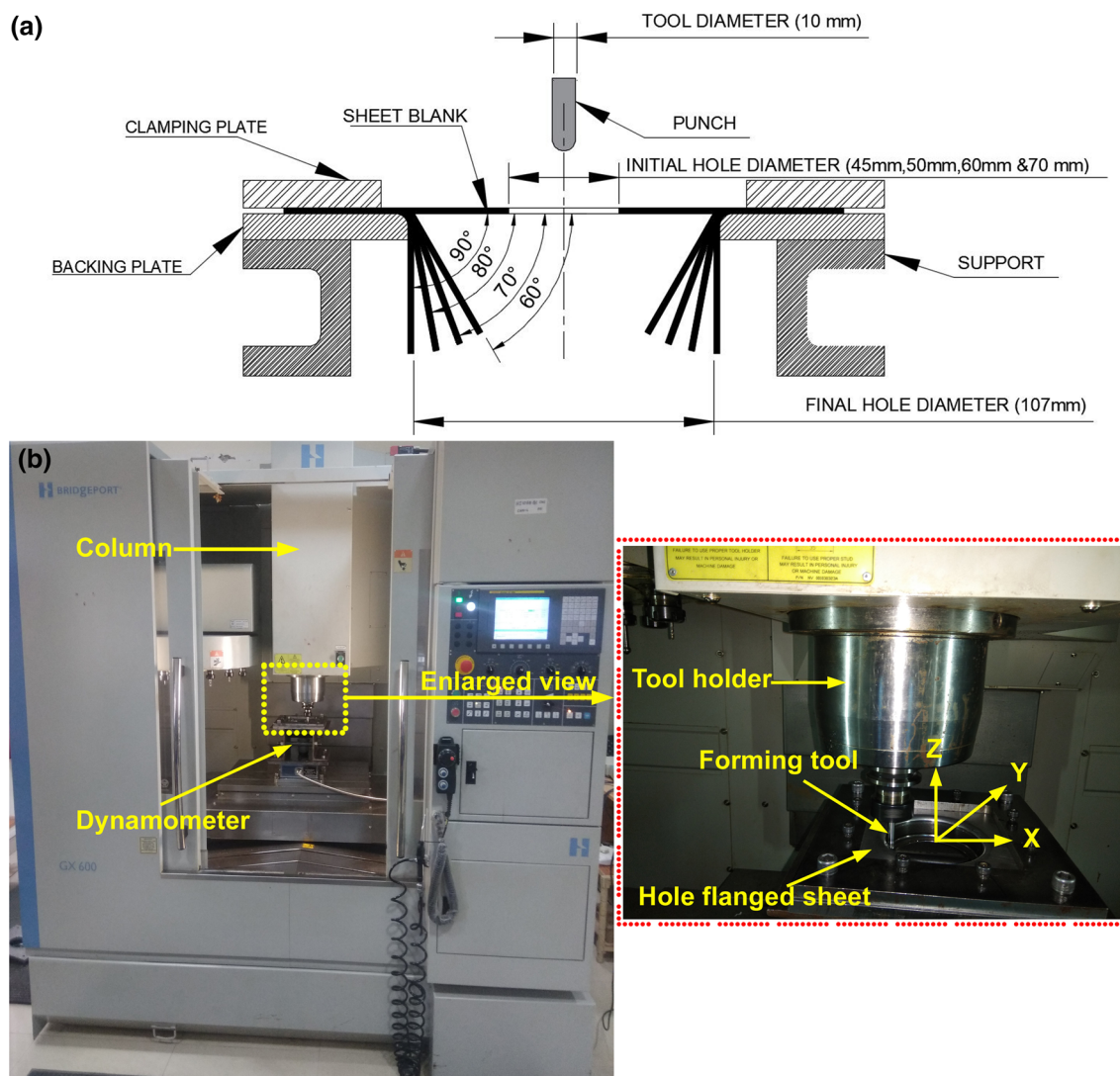
Fig. 1 **a** Schematic diagram of the IHF process, and **b** its corresponding experimental setup

Table 2 Experimental plan for multi-stage IHF process

Pre-cut hole diameter (mm)	Tool diameter (mm)	Forming strategies for multi-stage IHF			
		1st	2nd	3rd	4th
Ø45	10	60°	70°	80°	90°
Ø50		60°	70°	80°	90°
Ø60		60°	70°	80°	90°
Ø70		60°	70°	80°	90°

deformed IHF were cut along the RD-TD plane and mounted using copper conductive powder. Furthermore, the mounted samples were polished mechanically using SiC papers of decreasing granulometry, and diamond paste (3 mm) was used prior to colloidal silica (1 mm) polishing according to the standard procedure [33]. The specimens were then electrochemically etched using A2 electrolyte for 24 s at 35 V. The A2 electrolyte is a solution comprising of 78 mL perchloric acid, 90 mL distilled water, 730 mL ethanol, and 100 mL of butoxyethanol [34]. Finally, ultrasonic cleaning with ethanol was done on the electrochemically etched samples before placing them in the field emission scanning electron microscopy (FESEM). Orientation imaging was acquired using the electron backscattered diffraction (EBSD) technique.

Surface roughness tests using Taylor Hubson Talysurf were carried out to understand the quality of the IHF component. The critical parameter arithmetic mean of surface roughness (R_a) was considered to assess the surface quality of the product. The specimens were cut using the EDM machining process to avoid eventual errors in conical geometry. The roughness was measured perpendicular to

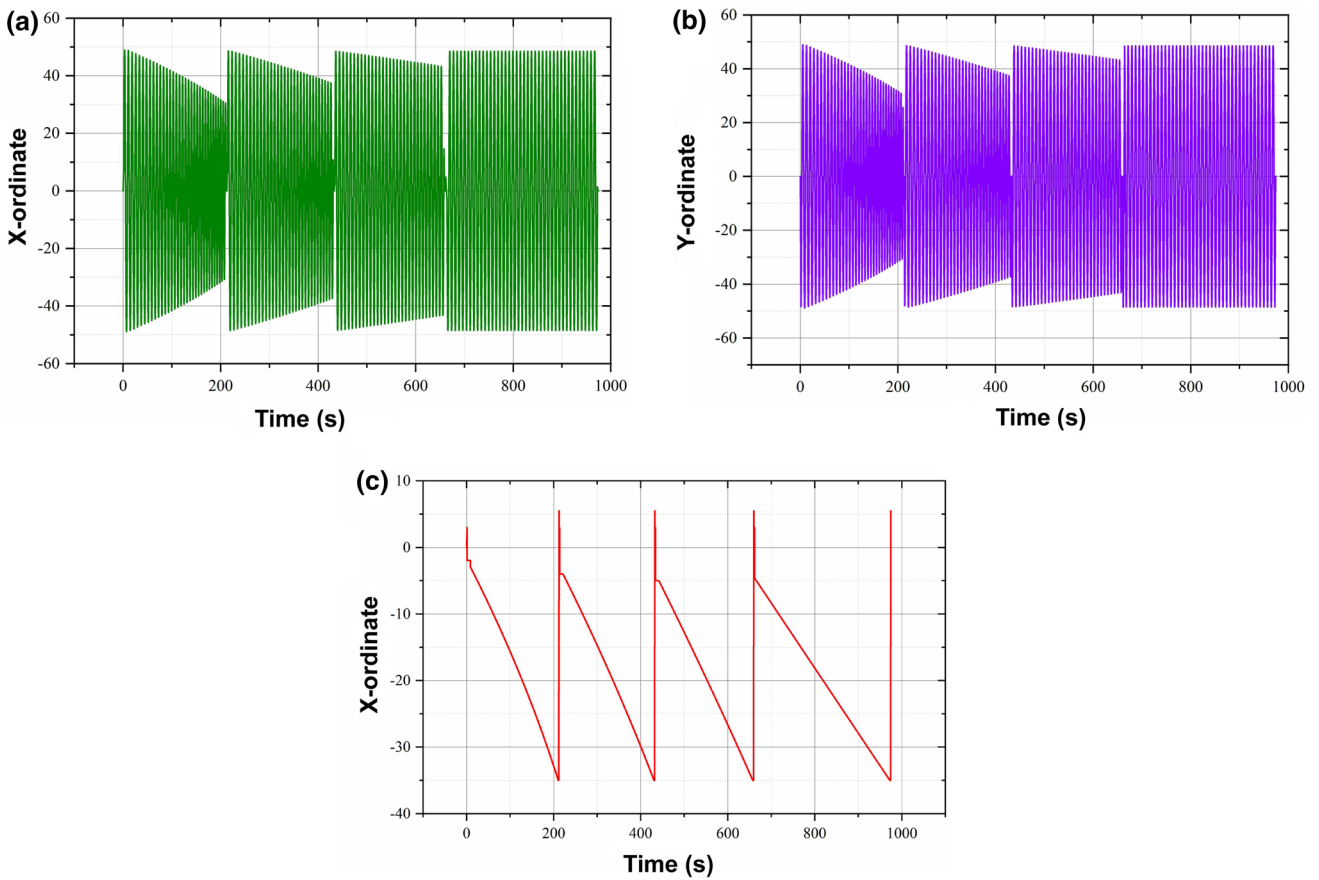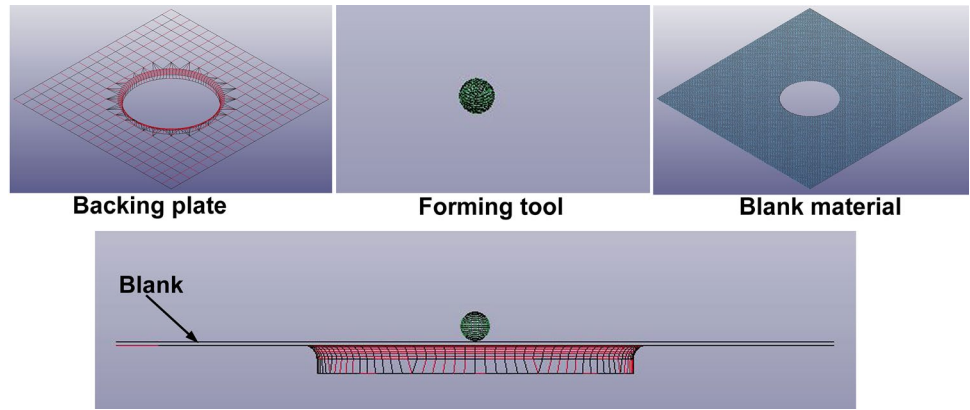**Fig. 2** Finite element model of incremental hole flanging process

Backing plate   Forming tool   Blank material

Fig. 3 Time versus position data for **a** *X*, **b** *Y* and **c** *Z* ordinate

the tool marks direction on the inner side of the formed parts. The cut-off length and sampling lengths for all the measurements are set as 0.8 mm and 4 mm, respectively. Three measurements were taken for each sample at different locations to ensure the repeatability of the measurement. The average value of the three readings was considered as the roughness value of the formed component.

3 Numerical analyses for ductile fracture

The constitutive equations associated with Hill 48 yield criterion under plane stress conditions $\sigma_3 = 0$ was used to define the anisotropic potential of the material, as shown in Eq. 7.

$$\sigma_{\text{Hill}} = \bar{\sigma} = \sqrt{\sigma_1^2 + \frac{r_0(1 + r_{90})}{r_{90}(1 + r_0)}\sigma_2^2 - \frac{2r_0}{1 + r_0}\sigma_1\sigma_2}. \qquad (7)$$

By using the associative flow rule, $d\bar{\varepsilon} = d\lambda\frac{\partial\bar{\sigma}}{\partial\sigma}$ in Eq. 7, the relationship between strain ratio $\left(\alpha = \varepsilon_2/\varepsilon_1\right)$ and stress ratio $\left(\beta = \sigma_2/\sigma_1\right)$ can be established as presented in Eq. 8.

$$\alpha = \frac{r_0}{r_{90}}\left[\frac{\beta - r_{90}(1 - \beta)}{1 + r_0(1 - \beta)}\right] \qquad (8)$$

Using total plastic work per unit volume in the account and imposing plane stress conditions, the term ξ can be evaluated as represented by Eq. 9.

$$\xi = \frac{d\bar{\varepsilon}}{d\varepsilon_1} = \frac{(1 + \alpha\beta)\left(\sqrt{r_{90}(1 + r_0)}\right)}{\left(\sqrt{r_{90} + r_0\beta^2 + r_0 r_{90}(1 - \beta)^2}\right)}. \qquad (9)$$

From the knowledge of ξ, the $\left(\bar{\sigma} = \sigma_{\text{Hill}}\right)$ can be estimated using Hollomon hardening law [35]. Further, χ which represents the ratio of major principal stress (σ_1) to the effective stress can be estimated (Eq. 10).

$$\chi = \frac{\sigma_1}{\bar{\sigma}} = \frac{1}{\left(\sqrt{\frac{r_{90} + r_0\beta^2 + r_0 r_{90}(1-\beta)^2}{r_{90}(1+r_0)}}\right)}. \qquad (10)$$

Stress triaxiality (η) is extensively used in fracture prediction. It is expressed as the ratio of hydrostatic stress $\left(\sigma_m = (\sigma_1 + \sigma_2)/3\right)$ to the effective stress $\left(\bar{\sigma} = \sigma_{\text{Hill}}\right)$, as shown in Eq. 11.

$$\eta = \frac{\sigma_m}{\bar{\sigma}} = \frac{1}{3} \times \frac{(1 + \beta)}{\left(\sqrt{\frac{r_{90} + r_0\beta^2 + r_0 r_{90}(1-\beta)^2}{r_{90}(1+r_0)}}\right)}. \qquad (11)$$

The commonly used models to predict ductile fracture are presented in Table 3. These criteria are simple and with one material constant, in which fracture occurs when a stress function over the effective strain field reaches a critical value [12, 36–38].

In all these fracture theories, $\bar{\varepsilon}_f$ is the equivalent plastic strain to fracture, and C_{CL}, C_{MC}, C_{RT}, C_{BR}, C_{OH} and C_{KO} are material constants. It is important to note that the experimental failure limit was considered as a reference to check the prediction accuracy.

4 Results and discussion

4.1 Limiting forming ratio

A series of multi-stage IHF experiments were performed as per Table 2. Figure 4 represents the successful and unsuccessful cylindrical flanges formed at the last stage of the multi-stage IHF process for a particular initial pre-cut hole diameter. The formability parameters such as flange height (h), final diameter (d_f), and HER of the formed part at different wall angles are presented in Table 4. Irrespective of the stage, an increase in the pre-cut hole diameter showed a decrease in the flange height and HER value. The increase in flange height in a smaller pre-cut hole diameter responsible for the progressive thinning of the sheet, which resulted in a premature fracture. The maximum LFR of 2.06 is observed at a pre-cut hole diameter of 50 mm, a wall angle of 90°, and a minimum value of 1.17 at 70 mm and 60°. In the process of finding the LFR using multi-stage ISF, a crack initiated around the periphery of the flange for 45 mm pre-cut hole diameter at a wall angle of 80°, as shown in Fig. 4a.

The theoretical height of the cylindrical flange (wall angle 90°) in IHF is $(d_f - d_i)/2$. Accordingly, the theoretical height of the cylindrical flange with a pre-cut hole of 70 mm, 60 mm, and 50 mm diameter will be 20 mm, 25 mm, and 30 mm respectively. However, the experimentally flange heights were obtained as 22 mm, 34 mm, and 50 mm respectively. These results indicate that there was a severe stretching in the flange with an increase in pre-cut hole diameter. However, the stretching is minimal with a 70 mm diameter hole. When the diameter of the pre-cut hole is 50 mm, the flange was stretched substantially by 66.66%. This excessive stretching in the meridional direction led to a considerable reduction in the thickness of the flange. In spite of that, failure in the 50 mm pre-cut hole diameter did not occur; however, the flange may not be acceptable in actual manufacturing due to the constraints on minimum wall thickness. In addition to that, alternative strategies need to be developed to improve thickness distribution in the flange wall. Moreover, it is noteworthy that thinning/stretching was negligible when the theoretical flange height is less than or equal to 20 mm. Thus, any new strategy that will be developed to improve the thickness distribution in hole flanging should be validated for cylindrical flanges with a theoretical flange height of more than 20 mm.

From the above discussion, it is evident that the flange thickness is also an essential parameter apart from the LFR to assess the formability or usefulness of the product. The average thickness of the formed flange as the function of non-dimensional parameter h/d_f and HER represented as Eq. 18.

Table 3 List of ductile fracture models used in the present work

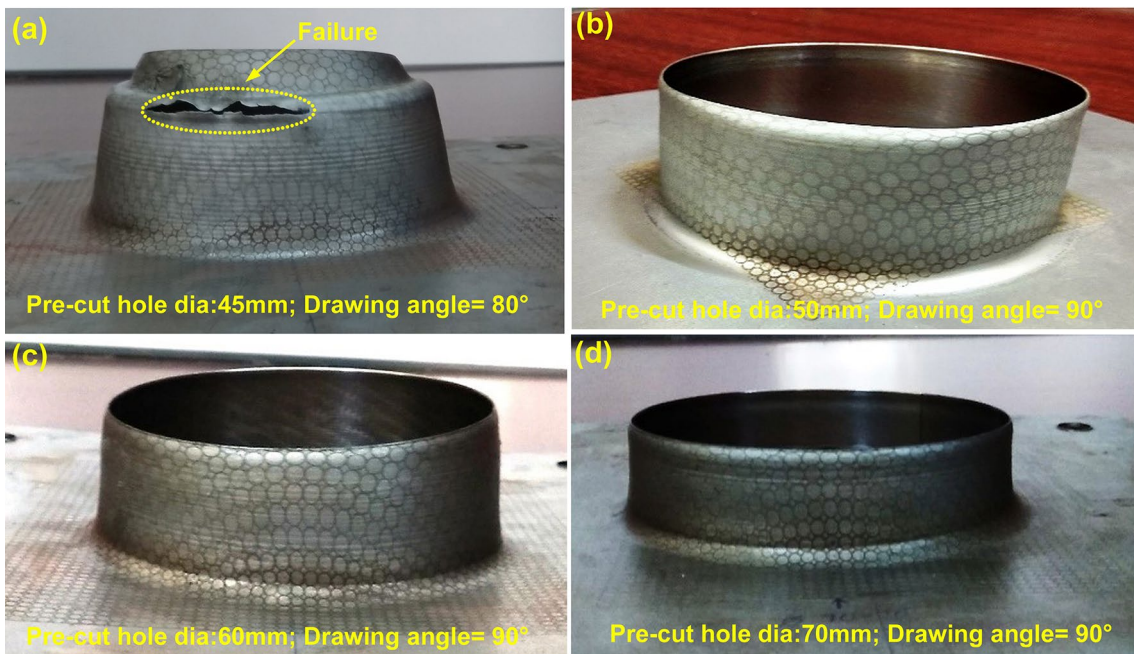| Ductile fracture models	Mathematical formulation
Cockcroft and Latham (C_{CL}) [39]	$$\int_0^{\bar{\varepsilon}_f} \sigma_{\max} d\bar{\varepsilon} = \int_0^{\bar{\varepsilon}_f} \frac{\sigma_1}{\bar{\sigma}} \cdot \bar{\sigma} \cdot \frac{d\bar{\varepsilon}}{d\bar{\varepsilon}_1} \cdot d\bar{\varepsilon}_1 = \int_0^{\bar{\varepsilon}_f} \chi \cdot \bar{\sigma} \cdot \xi \cdot d\bar{\varepsilon}_1 = C_{CL} \quad (12)$$
Ayyada (C_{AY}) [40, 41]	$$\int_0^{\bar{\varepsilon}_f} \left(\frac{\sigma_m}{\bar{\sigma}} \right) d\bar{\varepsilon} = \int_0^{\bar{\varepsilon}_f} \left(\frac{\sigma_m}{\sigma_1} \cdot \frac{\sigma_1}{\bar{\sigma}} \right) \frac{d\bar{\varepsilon}}{d\bar{\varepsilon}_1} d\bar{\varepsilon}_1 = \int_0^{\bar{\varepsilon}_f} \left(\frac{1+\beta}{3} \right) \cdot \chi \cdot \xi \cdot d\bar{\varepsilon}_1 = C_{MC} \quad (13)$$
Rice and Tracey (C_{RT}) [42]	$$\int_0^{\bar{\varepsilon}_f} 0.283 \ \exp\left(\frac{3\sigma_m}{2\bar{\sigma}} \right) d\bar{\varepsilon} = \int_0^{\bar{\varepsilon}_f} 0.283 \ \exp\left(\frac{3}{2} \cdot \frac{\sigma_m}{\sigma_1} \cdot \frac{\sigma_1}{\bar{\sigma}} \right) \frac{d\bar{\varepsilon}}{d\bar{\varepsilon}_1} \cdot d\bar{\varepsilon}_1$$ $$= \int_0^{\bar{\varepsilon}_f} 0.283 \ \exp\left(\left(\frac{1+\beta}{2} \right) \cdot \chi \right) \cdot \xi \cdot d\bar{\varepsilon}_1 = C_{RT} \quad (14)$$
Brozzo et al. (C_{BR}) [43]	$$\int_0^{\bar{\varepsilon}_f} \frac{2\sigma_1}{3(\sigma_1 - \sigma_m)} d\bar{\varepsilon} = \int_0^{\bar{\varepsilon}_f} \frac{2}{3(1 - \sigma_m/\sigma_1)} \cdot \frac{d\bar{\varepsilon}}{d\bar{\varepsilon}_1} \cdot d\bar{\varepsilon}_1$$ $$= \int_0^{\bar{\varepsilon}_f} \frac{2}{(2 - \beta)} \cdot \xi \cdot d\bar{\varepsilon}_1 = C_{BR} \quad (15)$$
Oh et al. (C_{OH}) [44]	$$\int_0^{\bar{\varepsilon}_f} \left(\frac{\sigma_{\max}}{\bar{\sigma}} \right) d\bar{\varepsilon} = \int_0^{\bar{\varepsilon}_f} \left(\frac{\sigma_1}{\bar{\sigma}} \right) \cdot \frac{d\bar{\varepsilon}}{d\bar{\varepsilon}_1} \cdot d\bar{\varepsilon}_1 = \int_0^{\bar{\varepsilon}_f} (\chi) \cdot \xi \cdot d\bar{\varepsilon}_1 = C_{OH} \quad (16)$$
Ko et al. (C_{KO}) [36]	$$\int_0^{\bar{\varepsilon}_f} \frac{\sigma_1}{\bar{\sigma}} \left\langle 1 + \frac{3\sigma_m}{\bar{\sigma}} \right\rangle d\bar{\varepsilon} = \int_0^{\bar{\varepsilon}_f} \frac{\sigma_1}{\bar{\sigma}} \left\langle 1 + 3 \cdot \frac{\sigma_m}{\sigma_1} \cdot \frac{\sigma_1}{\bar{\sigma}} \right\rangle \cdot \frac{d\bar{\varepsilon}}{d\bar{\varepsilon}_1} \cdot d\bar{\varepsilon}_1$$ $$= \int_0^{\bar{\varepsilon}_f} \chi \langle 1 + (1+\beta) \cdot \chi \rangle \cdot \xi \cdot d\bar{\varepsilon}_1 = C_{KO} \quad (17)$$

Fig. 4 Incremental hole flanging successful and unsuccessful formed components

Table 4 Summary of results from multi-stage IHF with different diameters of pre-cut holes

Pre-cut hole dia	Intermediate stages	h (mm)	d_f (mm)	h/d_f	HER
ϕ45	Stage 1 (60°)	40	58.5	0.68	1.30
ϕ50		38	67.3	0.56	1.30
ϕ60		25	77	0.36	1.26
ϕ70		18	82.5	0.22	1.17
ϕ45	Stage 2 (70°)	44.5	66	0.67	1.46
ϕ50		40	76.5	0.52	1.53
ϕ60		29	87.3	0.33	1.41
ϕ70		20	92	0.21	1.31
ϕ45	Stage 3 (80°)	–	–	–	–
ϕ50		43	88.8	0.48	1.78
ϕ60		32	96.6	0.33	1.58
ϕ70		21	99	0.21	1.41
ϕ45	Stage 4 (90°)	–	–	–	–
ϕ50		50	103.3	0.48	2.06
ϕ60		34	103.5	0.39	1.73
ϕ70		22	105	0.20	1.51

$$t_{ave} = \frac{1 - 1/\text{HER}^2}{4\left(h/d_f\right)} \times t_0. \tag{18}$$

From the above equation, the average flange thickness for DDQ steel blanks with a pre-cut hole diameter of 70 mm, 60 mm, and 50 mm is 0.66 mm, 0.47 mm, and 0.39 mm respectively. These results indicate that the average flange thickness is decreasing with an increase in LFR. The flanges were formed successfully with vertical walls in all blanks with pre-cut hole diameter is greater than or equal to 50 mm. When the diameter of the hole is 45 mm, the flange was formed successfully up to 70° wall angles. A circumferential crack was observed towards the middle of the flange with 80° wall angle. This circumferential cracking is very similar to the circumferential failure in conventional ISF under plane strain conditions. The 80° wall angle at the failure in IHF is also very close to the maximum wall angle 77° that can be formed for deep drawing quality steels in conventional ISF. This observation indicates that the plastic flow of material in the IHF process approaches the conventional ISF with a decrease in the hole diameter.

4.2 Formability limit

The formability of material in the ISF process is better than the conventional deep drawing and stretching process due to suppressed necking [45]. Therefore, forming limit diagram (FLD) obtained using conventional methods shows limitation to assess the material formability during the multi-stage ISF process. Thus, the fracture forming limit diagram

(FFLD) is utilized for the formability analysis in the IHF process. Theoretically, FFLD is a straight line in principal strain space with a negative slope (− 1) as given by Eq. 19

$$\varepsilon_{1f} + \varepsilon_{2f} = -\varepsilon_{3f}. \tag{19}$$

The process of constructing FFLD is more complex than FLD. The experimental procedure to construct the FFLD requires measuring thickness before and after fracture along the crack and necking strain under different strain paths. The necking and fracture thickness strain under different strain paths is obtained from the Nakazima test by deforming rectangular blanks with different widths using a hemispherical punch. The details of the tests are mentioned elsewhere [34]. Many researchers have reported that the material undergoes plane strain deformation from necking to fracture without any appreciable lateral strain in the material [38]. Based on this assumption second minor principal strain at fracture (ε_{2f}) is equivalent to the minor principal strain at necking (ε_{2n}). The strains in the necking zone can be obtained from circle grid analysis (CGA) of blanks formed in Nakazima test. The third principal fracture strain in thickness direction is obtained by measuring fracture thickness (t_f) and initial thickness of blank (t_0) using the $\varepsilon_{3f} = \ln\left(\frac{t_f}{t_0}\right)$ relation. Finally, the major principal fracture strain obtained from volume consistency relation given as Eq. 20

$$\varepsilon_{1f} = -\varepsilon_{2n} - \ln\left(\frac{t_f}{t_0}\right). \tag{20}$$

However, this conventional procedure to construct the FFLD is a time-consuming process. In this regard, Isik et al. [46] proved that the FFLD obtained by measuring the fracture strains in varying wall angle conical and pyramidal frustums formed in ISF is very close to the FFLD obtained from the conventional forming test. Therefore, continuously varying wall angle conical frustum (VWACF) and varying wall angle pyramidal frustum (VWAPF) were used in the present work to obtain the FFLD of the material [47]. VWACF and VWAPF are formed by a 10 mm diameter hemispherical headed tool on three-axis CNC milling machine till the fracture. The fracture strains are evaluated using the above equations, and the detailed procedure is described elsewhere [48]. Figure 5a, b represents the experimentally deformed VWACF and VWAPF components, and the fracture strains ($\varepsilon_{1f}, \varepsilon_{2f}$) are found to be (0.06, 1.52) and (0.4, 1.15), respectively. The in-plane fracture strains obtained from VWACF and VWAPF are shown in Fig. 5b, and a straight line is fitted to get the FFLD. The resultant FFLD can be given by Eq. 21. A safe limit of 10% is considered to account for experimental uncertainty.

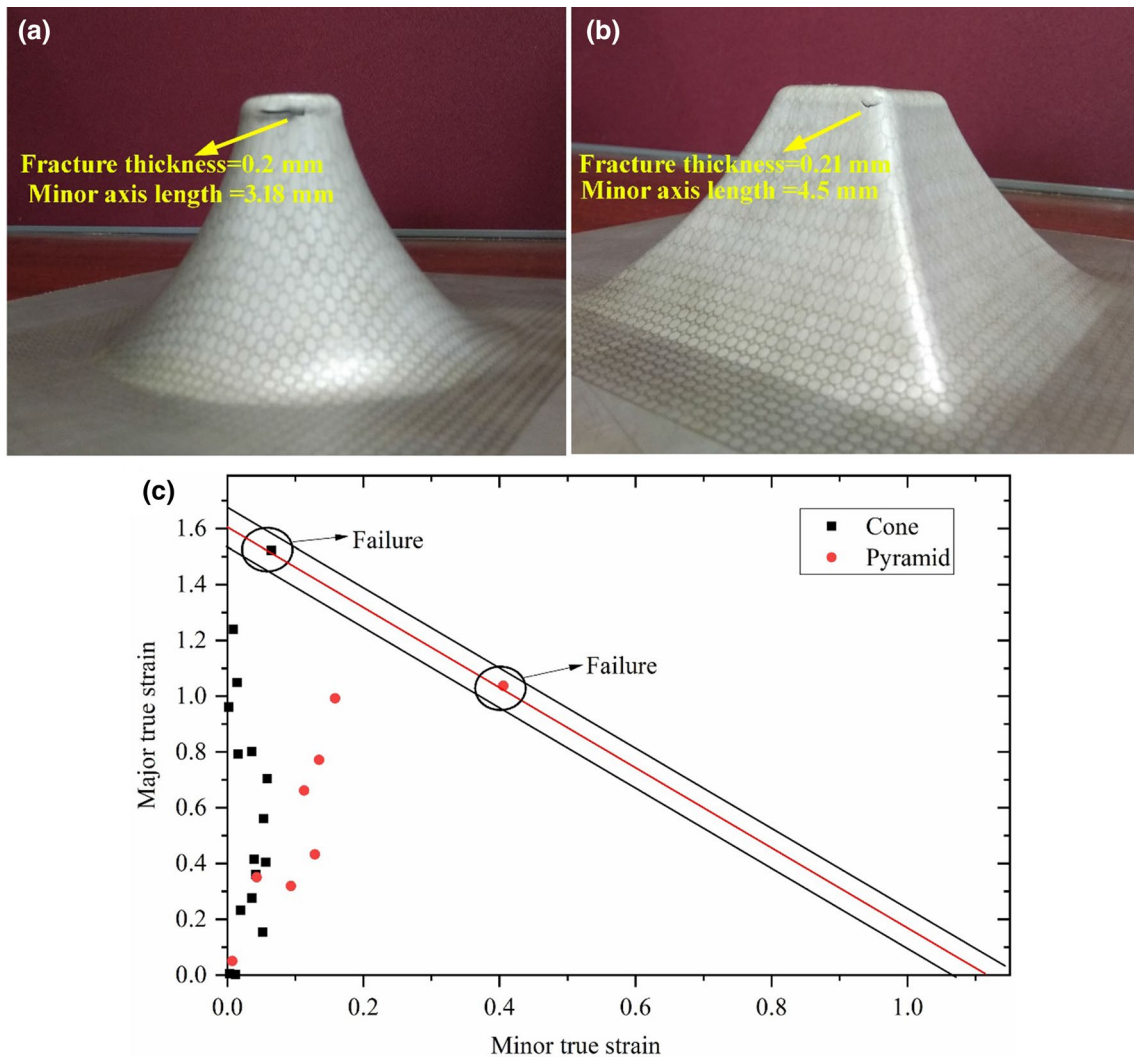$$\varepsilon_{1f} - 1.04\varepsilon_{2f} = 1.58. \tag{21}$$

Fig. 5 Deformed component of **a** varying wall angle conical frustum (VWACF), **b** varying wall angle pyramidal frustum (VWAPF), and **c** experimental FFLD for cone and pyramid

From the above equation, the fracture strain under the plane strain (FLD_0) condition was found to be 1.58. The maximum wall angle (ψ_{max}) corresponds to this fracture strain was estimated using Eq. 22 and is equal to 78° [49]. This value is in good agreement with the maximum formable wall angle of 77° obtained from experiments. Further, the theoretical slope of the FFLD is − 1. The actual slope (m) of FFLD considering tool radius (r_{tool}) and sheet thickness (t) was calculated using Eq. 23 and is found to be − 1.09. The difference in slope between experimental and theoretical predictions is only 3.8%.

$$FLD_0 = \ln\left(\frac{\pi}{2} - \psi_{max}\right), \tag{22}$$

$$m = \frac{5(r_{tool}/t) - 2}{3(r_{tool}/t) + 6}. \tag{23}$$

4.3 Comparison of theoretical models for predicting fracture loci

The material constants determined for different ductile fracture models are mentioned in Fig. 6. These material constants are employed to predict FFLDs based on the theory of proportional loading. To evaluate the predictability of various ductile fracture criteria, predicted FFLDs are compared with experimental results, as represented in Fig. 6. It is evident from the figure that all the models underestimate major fracture strains on the tension–compression side of FFLD. However, failure limits predicted by the Ayyada
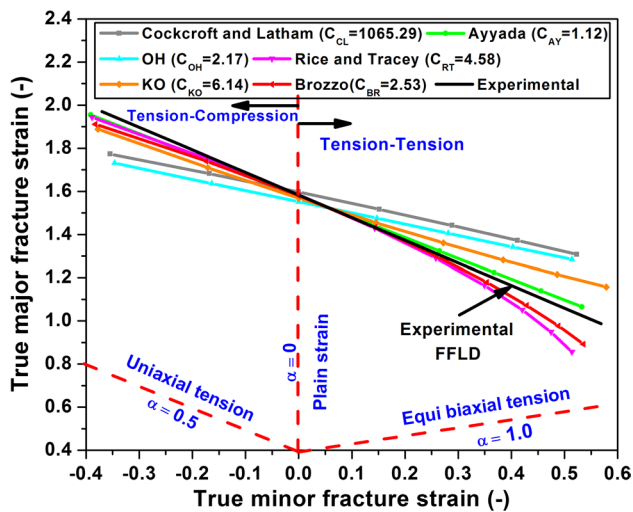
Fig. 6 Failure limit calibration of various ductile fracture criteria implementing Hills48 yield model

fracture criterion showed comparatively higher accuracy than other ductile fracture models. Near to plane strain condition, the major fracture strains predicted by all the ductile fracture models merged to a nearly single point. The deviations were found to be in the range of 2–5%, which describes the predicted fracture strain with high accuracy with experimental data. On the tension–tension side, ductile fracture criteria such as CL, AY, OH, and KO model overestimate facture limits, whereas RT and BR model underestimated the experimental data. Overall, the AY model demonstrates better prediction capability of failure limits as compared to other models. Moreover, the AY model did predict the fracture limit almost matching trend throughout the strain ratio domain ranging from the uniaxial tension to balanced biaxial tension. Henceforth, the AY model and experimentally obtained FFLD was considered for formability prediction in terms of strain path evolution, vertical forces, and thickness distribution.

4.4 Strain path evolution

The experimentally obtained FFLD and predicted AY model FFLD was considered as a failure limit for all the simulations. Figure 7 shows the strain path evolution for different pre-cut hole diameter and stages for experimental conditions mentioned in Table 2. It is observed from the figure that the major principal strains in all the stages with different pre-cut hole diameters are well below the FFLC, except Fig. 7c. The observation is in good agreement with the experimental results where the fracture is observed in the third stage with a pre-cut hole diameter of 45 mm diameter (refer Fig. 4a). The fracture was initiated near the middle of the flange and propagated towards

the circumferential direction due to the excessive stresses along the meridional direction. Hence, it is clear that the proposed simulations well predicted the fracture in the multi-stage IHF process. However, to validate further, the strain distribution obtained from simulations were compared with the major and minor principal strains measured from three different zones of formed geometry using the CGA technique. In CGA, small circles of 3 mm diameter are etched on the blanks with a pre-cut hole. After hole flanging operation, the initial circles are deformed into ellipses, and corresponding major and minor strains are evaluated using Eqs. 5 and 6.

Figure 8 shows the major and minor principal strains in the flange region for 60 mm pre-cut hole at different forming stages. The corresponding FE simulated cups showing major principal strains are shown in Fig. 9. The strain distribution pattern can be divided into three zones, as shown in Fig. 8a. In zone 1, the material is undergoing deformation near to plane strain mode. The major deformation has occurred in the meridional direction and negligible strains in the circumferential direction. The major strain is increasing with depth, and the minor strain shifted to the right-hand side negligibly. In zone 2, the major strain is decreasing, and the minor strain is increasing. In this zone, the deformation is shifting from plane strain to biaxial stretching mode.

In zone 3, the major strain is slightly increasing, and there is a reduction in minor strain. The material deformation is approaching uni-axial tension in the circumferential direction towards the edge of the pre-cut hole. The edges of the pre-cut holes are subjected to circumferential tension. With an increase in pre-cut hole diameter and number of stages, the overall strains shift towards the right side, as shown in Fig. 8b–d. In the case of zone 1, the maximum minor strains were shifted from 0.05 to 0.1 when the angle was increased from 60° to 70°. The maximum minor strain shift in zone 1 was found to be 200% and 300% when 80° and 90° angle was considered as compared to a 60° angle. It can be observed that the strain path along zone 1–2–3 obtained from the simulated results is in good agreement with the experimental results for all the conditions.

Further, all the strain paths in Fig. 7 are growing linearly from the origin to the maximum achievable strains in IHF irrespective of the wall angle and diameter of the initial pre-cut hole. This indicates that the material will fail by excessive thinning until fracture without any signs of localized necking. When there is a localized necking, the strain path is linear up to the FLD, and after that, it becomes a vertical line up to the FFLD. The vertical strain path is due to the plane strain mode of deformation in the material from the necking to fracture. However, there are no such changes in the strain path of the IHF process.
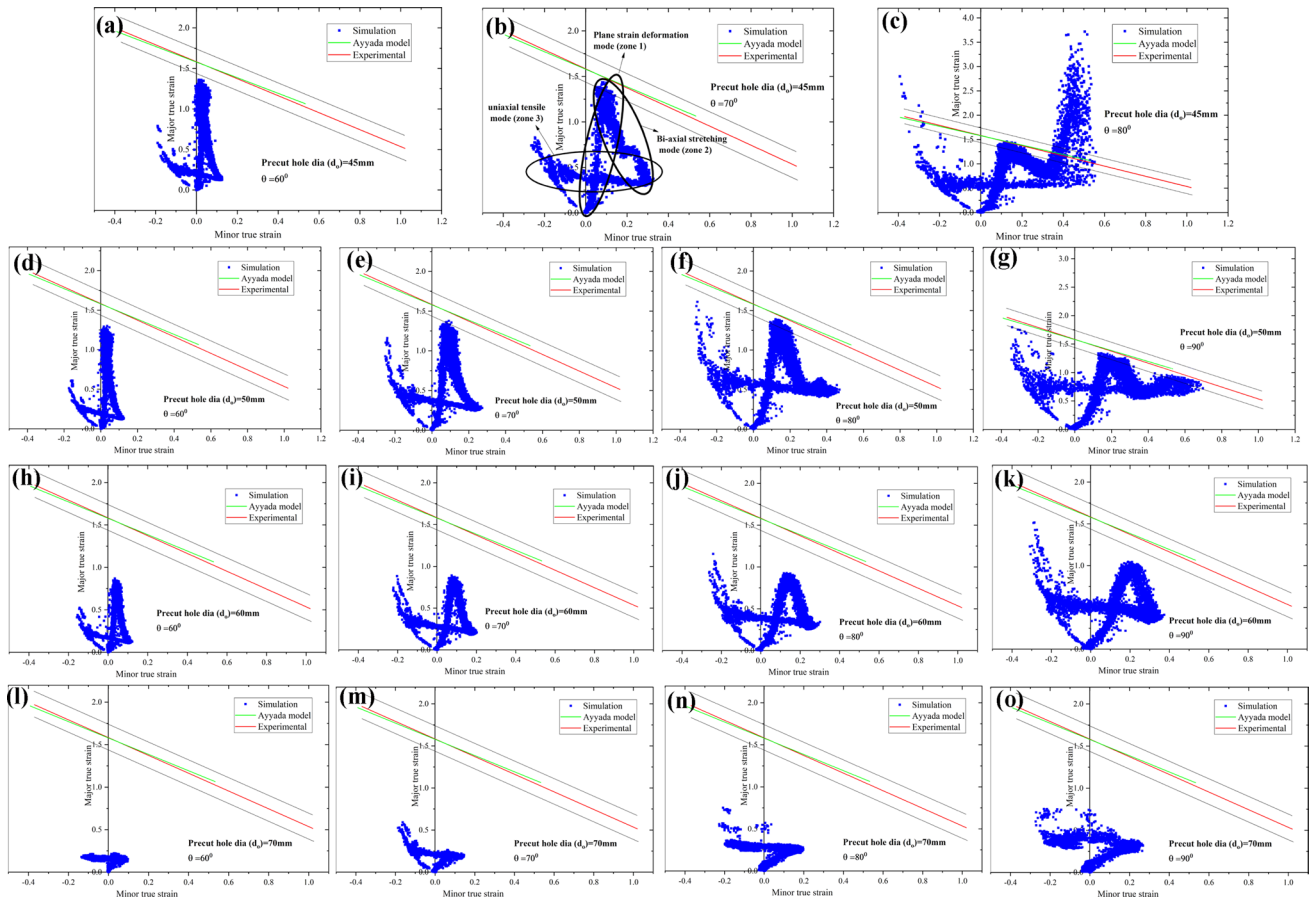
Fig. 7 FE predicted strain path evolution for different pre-cut hole diameters of **a–c** 45 mm, **d–g** 50 mm, **h–k** 60 mm, and **l–o** 70 mm with flanging stages

4.5 Formability prediction

4.5.1 Vertical force profile in IHF

Figure 10 depicts the comparison of simulated and experimentally encountered vertical forming force (F_z) during each stage with different pre-cut hole diameters. Irrespective of the pre-cut hole diameter, the vertical force is maximum in stage 1 due to the bending and stretching of the sheet over a large angle from 0° to 60°. The forming force is increased to maximum value steadily and then decreasing from a certain depth. The decrease in force with depth is due to the less stiffness of the sheet because of the pre-cut hole. This kind of force trend is different from the force curves observed in conventional ISF. In conventional ISF, the force reaches maximum value after initial bending around the backing plate corner radius and become steady throughout the forming operation unless thinning dominates the strain hardening of the material. Conversely, in the IHF process, the material offers less resistance to deformation due to the hole at the center of the blank; thereby, the force decreases from a certain depth. The maximum force in stage 1 is 1600 N

for blanks with pre-cut holes 45 mm, 50 mm, and 60 mm diameter on the other hand, the maximum force with 70 mm pre-cut hole is 1400 N. The decrease in force is due to less flange height and major influence of hole on the stiffness of the formed region.

The maximum force in the second stage was found to be 1100 N with 45 mm and 50 mm diameter of pre-cut holes. The force was 800 N and 600 N with 60 mm and 70 mm pre-cut hole diameters, respectively. The reduction of force in the second stage, irrespective of pre-cut hole diameter, is due to less deformation energy required for further deformation from 60° to 70° flange. Because of increased radial deformation and thickness of the flange towards the end of the flange, a combination of bending and stretching led to maximum force towards the edge of the hole in stage 1, whereas the deformation is predominately by stretching from the second stage onwards. There is a slight reduction in the forming forces in the subsequent stages. In the third stage, the forming forces are 900 N, 700 N, and 500 N for 50, 60, and 70 mm pre-cut hole diameters respectively. Despite an increase in strain hardening of material in the subsequent stages, thickness reduction and sheet stiffness in the axial
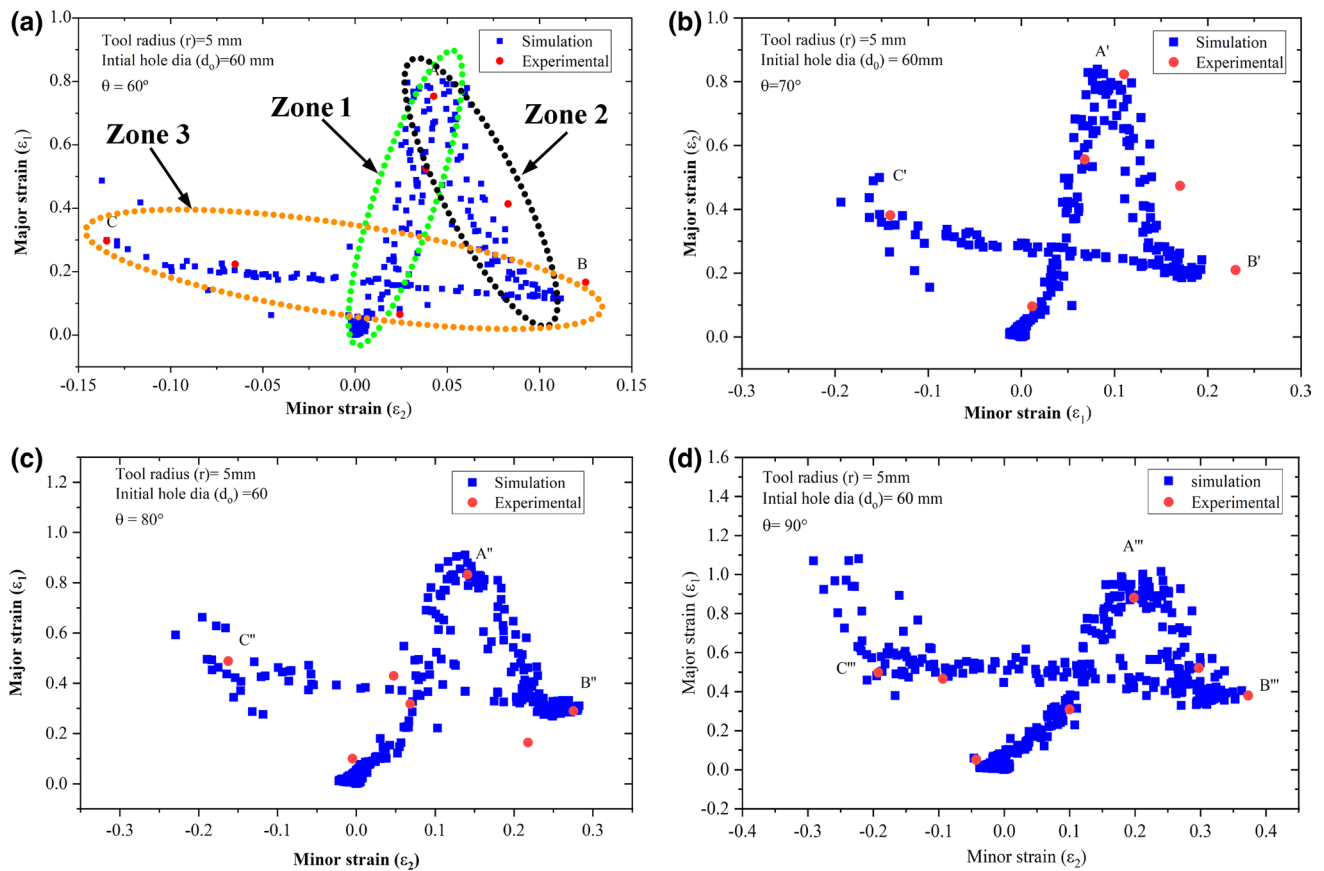
Fig. 8 FE predicted and experimental strain path for multi-stage IHF process for 60 mm pre-cut hole diameter at different flanging stages of **a** 60°, **b** 70°, **c** 80°, and **d** 90°

direction dominate, which eventually decreases the forming force. There is a crack after reaching the middle of the depth in the third stage of forming with a 45 mm pre-cut hole. It is evident from the simulations that the forming force trend in the third stage decreases from the point of initiation of crack. The forming forces in the fourth stage are found to be 600 N, 500 N, and 400 N for 50, 60, and 70 mm pre-cut hole diameters respectively. The decrease in the force could be due to the same reasons as mentioned for the third stage. Leu et al. [50] studied the forming forces in conventional hole flanging of 1 mm thick steel sheets with different shapes of punches. In their study, the forming forces were found to be varied between 20 kN to 40 kN with the different punch geometries. These forces are very high compared to forming forces in IHF. Further, the FE simulation results are in well agreement with the forming force trends of experimental data.

4.5.2 Wall thickness distribution

Figure 11 shows the thickness profiles of flanges obtained from numerical simulations in a multi-stage IHF process with different pre-cut hole diameters. The corresponding variation of major and minor principal strains in different zones with the depth of flange are shown in Fig. 12. In each sample, the thickness is decreasing to a minimum value and then increasing irrespective of pre-cut hole diameter. The decrease in thickness up to a certain depth of flange is due to the increase in major principal strain in zone-1. Therefore, the maximum thickness reduction has occurred towards the end of zone-1 (plane strain deformation zone). After this, the material is pushed downwards, and the thickness is increasing. The increase in thickness occurs in zone-2 (biaxial stretching zone) and zone-3 (uni-axial tension zone). In zone-2, the major principal strain is decreasing and the minor principal strain is increasing slightly therefore thickness strain should increase to satisfy the volume consistency relation. In zone-3, the major principal strain is increasing, but at the same time, the minor strain is decreasing; therefore, the thickness strain is increasing in zone-3.

The maximum thickness reduction in each stage with different pre-cut hole diameters is consolidated in Table 5. The results reveal that the percentage of thickness reduction increases with an increase in the number of stages. For a given stage number, thickness reduction
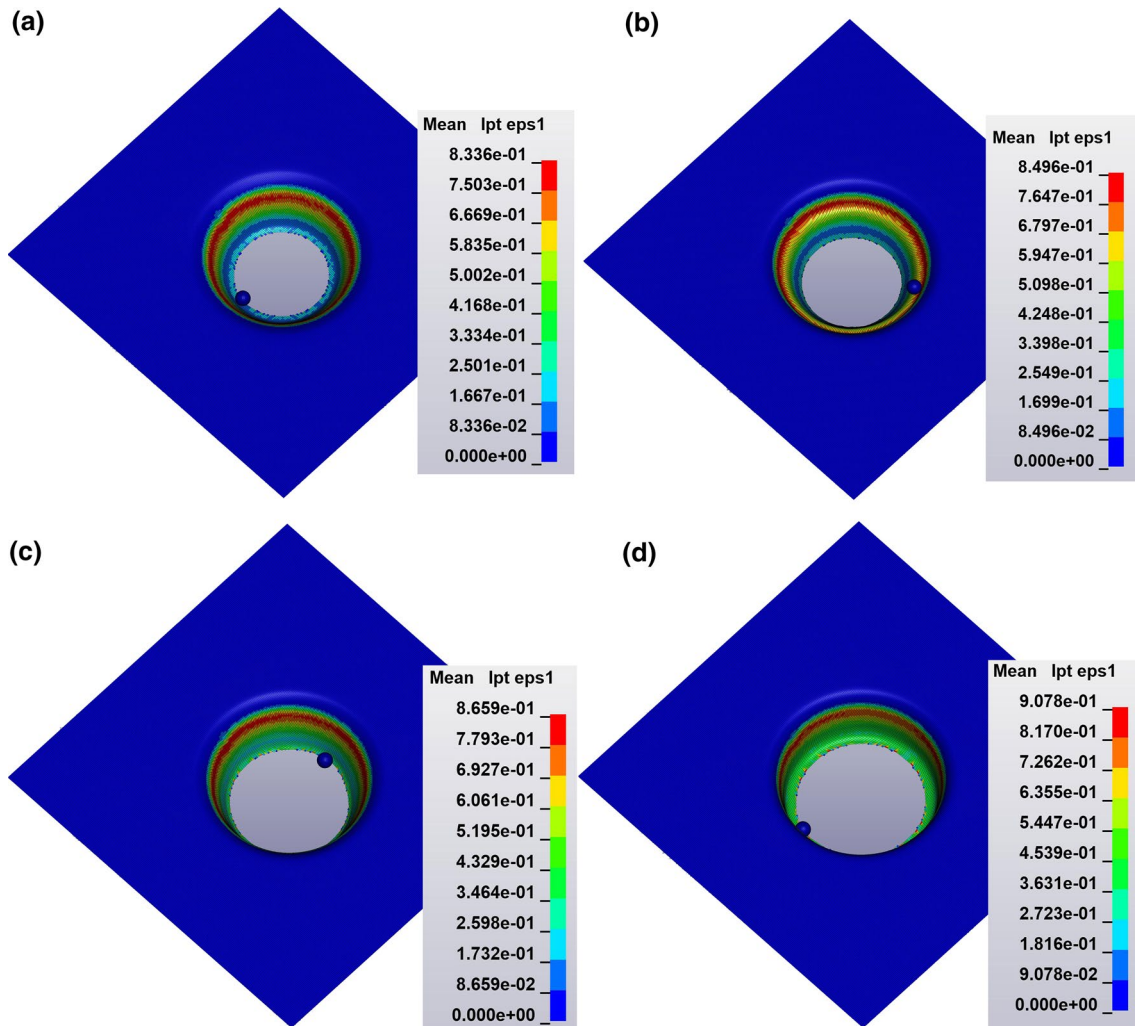
Fig. 9 FE simulated cup showing major principal strain profile for 60 mm pre-cut hole diameter at different flanging stages of **a** 60°, **b** 70°, **c** 80°, and **d** 90°

is increasing with a decrease in pre-cut hole diameter. The maximum thickness reductions are found to be 28%, 46%, 62%, and 66% for pre-cut hole diameters of 70 mm, 60 mm, 50 mm, and 45 mm respectively. Less thinning in large diameter hole is mainly due to the reduction of strains in the meridional direction.

To get more insight, the experimentally obtained thickness distribution result is compared with FE obtained thickness distribution for 60 mm pre-cut hole diameter at different stages as depicted in Fig. 13. The maximum thickness reduction in each stage is slightly shifting towards the right side in each subsequent stage of deformation, which occurred due to an increase in flange height in successive stages. The predicted thickness distribution showed the exact nature of experimental data with maximum error within the limit of 5%.

4.6 Post forming analyses

4.6.1 Micro-texture characterization

To get more insight into the occurrence of three different strain paths in the particular incremental flanging step and shift of strain path on subsequent steps, a 60 mm pre-cut hole diameter specimen with a flanging angle of 60° and 90° is considered. Figure 14 shows the specimen cut from the base material and different deformation zones for microtexture analyses. The inverse pole figure (IPF) at corresponding locations is presented in Fig. 15.

IPF map in Fig. 15a demonstrates that the DDQ grains at base material were coarse and bi-modal grain size distribution. The average grain size was observed to be approximately 88 μm. The average grain size decreased gradually
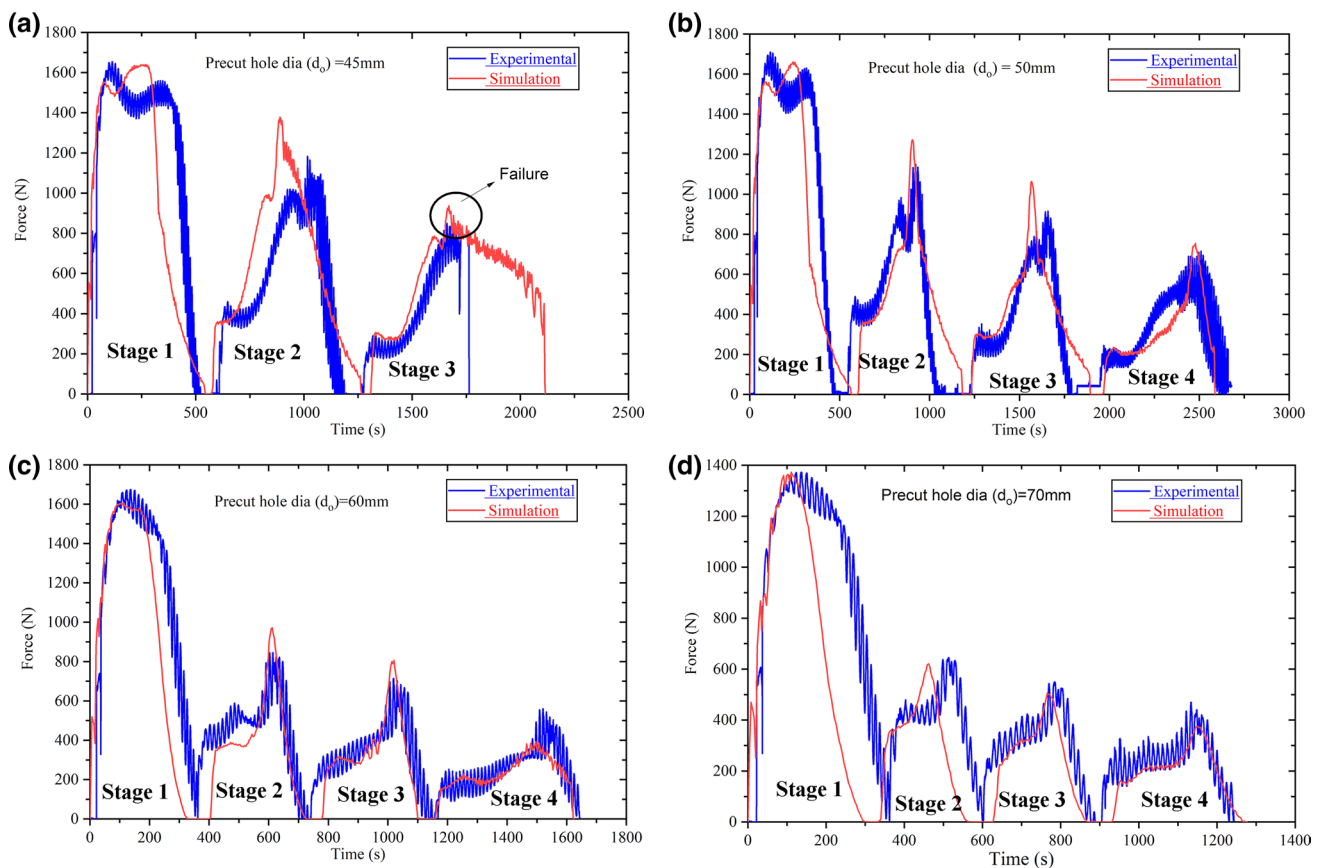
Fig. 10 Vertical forces encountered during the IHF process for pre-cut hole diameters of **a** 45 mm, **b** 50 mm, **c** 60 mm, and **d** 70 mm at different flanging stages

with subsequent deformation stages with respect to base material as shown in Fig. 15b–e. In this context, the distinction of grain size can be defined in terms of low-angle grain boundaries (LAGBs) and high angle grain boundaries (HAGBs) segment owing to their different capacities to act as a barrier to crack propagation and continuous dislocation flow. The misorientation angles less than 15° signifies the low angle grain boundaries (LAGBs), whereas greater than 15° denotes the high angle grain boundaries (HAGBs) [51, 52]. Misorientation angle graphs obtained for base material and different deformation zone is depicted in Fig. 16a–e. The consolidated LAGB and HAGB fraction for different conditions is presented in Fig. 16f. From the figures, it is evident that the decreasing trend in grain size with deformation occurred due to the increased density of low-angle grain boundaries (LAGBs). The misorientation angle established that the volume fraction of LAGBs increased from 0.4 in base material to 0.8 in the deformed sample, indicating an approximately 200% increase in fraction irrespective of the zone considered. This increase in LAGBs might have occurred due to the

generation of deformation bands at grain interior and dislocations activities during plastic deformation. The occurrence of these grain interior barriers subdivides the grain boundaries, leads to the formation of LAGBs as reported by Prasad et al. [52].

Further, the grains in the base material are found to be almost equally distributed towards the planes {111}, {101}, and {001}. This observation is in good agreement with the isotropic nature of the material as consolidated in Table 1. It was observed that the grains are more aligned towards the {111} and {101} plane with the increase in plastic deformation irrespective of the deformation zone considered. The grain boundaries associated with {111} and {110} planes improve fracture resistance, which provides further scope for plastic deformation [53]. It is also clearly visible from Fig. 15c, e that most of the grains are slightly elongated in one axis with respect to the plane strain condition in Fig. 15b. This elongation of grains in one axis might have led to biaxial straining and shifted the plain strain zone towards the biaxial deformation zone.
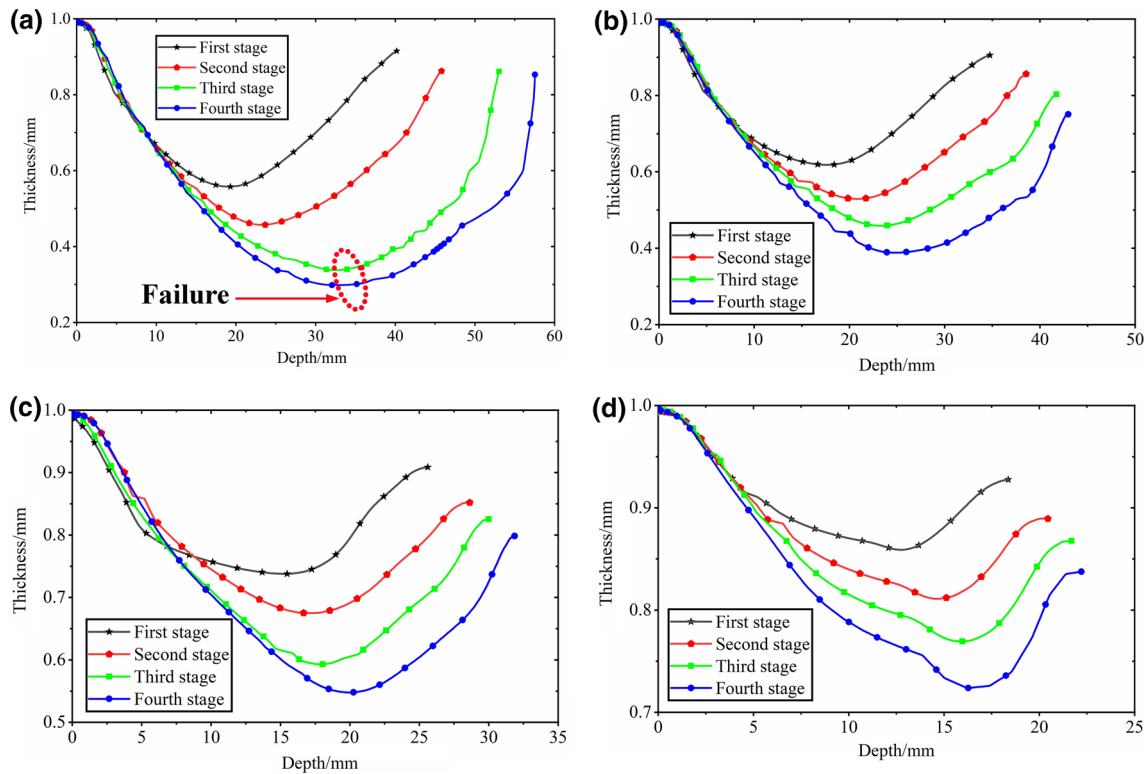
Fig. 11 FE predicted wall thickness distribution for all the deformation conditions

4.6.2 Surface roughness

The surface quality of the formed parts is a crucial aspect in sheet forming and is severely affected by several processes and material parameters such as forming strategies, lubrication, and sheet material. In the IHF process, the roughness gets affected by the vertical step size (d_z), tool diameter (R_t) and wall angle (α). The roughness of formed parts measured using Talysurf profilometer. Figure 17 shows the roughness profiles obtained for the specimen with a 60 mm pre-cut hole diameter formed by a tool with a 5 mm radius. The surface roughness of the undeformed blank was found to be 1.38 μm. At the end of the first stage, the surface roughness of the 60° conical inner surface flange was decreased from 1.38 to 1.15 μm, showing a decrease of approximately 17%. This decrease in surface roughness might have occurred due to the stick–slip motion of the IHF tool on the sheet surface.

The surface roughness of the vertical flange was found to be 0.9 μm, 0.72 μm, and 0.65 μm when the wall angle of the formed parts is increased to 70°, 80° and 90°, respectively. The surface roughness of the final formed surface showed an improvement of 53% compared to the undeformed base material. Similarly, surface roughness values are obtained from deformed 45 mm, 50 mm, 70 mm pre-cut hole diameter. The results indicated a similar trend of decrease in surface roughness with an increase in the number of forming

steps. The improvement in surface quality has been attributed to reducing friction in the formed surfaces. The increase in the number of passes ensures that all the surface asperities are compressed due to increased burnishing action between the forming tool and sheet, leading to an improvement in the surface finish.

5 Conclusions

The capability of the multi-stage IHF process to produce cylindrical flanges has been analyzed through successful experiments and finite element simulations. The experiments have been performed on 1 mm thick DDQ steel sheets with a pre-cut hole diameter of 45 mm, 50 mm, 60 mm, and 70 mm. The flange was formed in four stages, with an initial angle of 60° to 90° with an angular increment of 10°. The main conclusions from the present work are summarized as follows.

- The maximum limiting forming ratio (LFR) of 2.06 was obtained with a pre-cut hole diameter of 50 mm. However, LFR alone cannot assess the formability in IHF due to severe thinning and an increase in flange height compared to the conventional hole flanging process (CHF).
- The fracture forming limit (FFLD) of DDQ steel was experimentally determined and can be described as
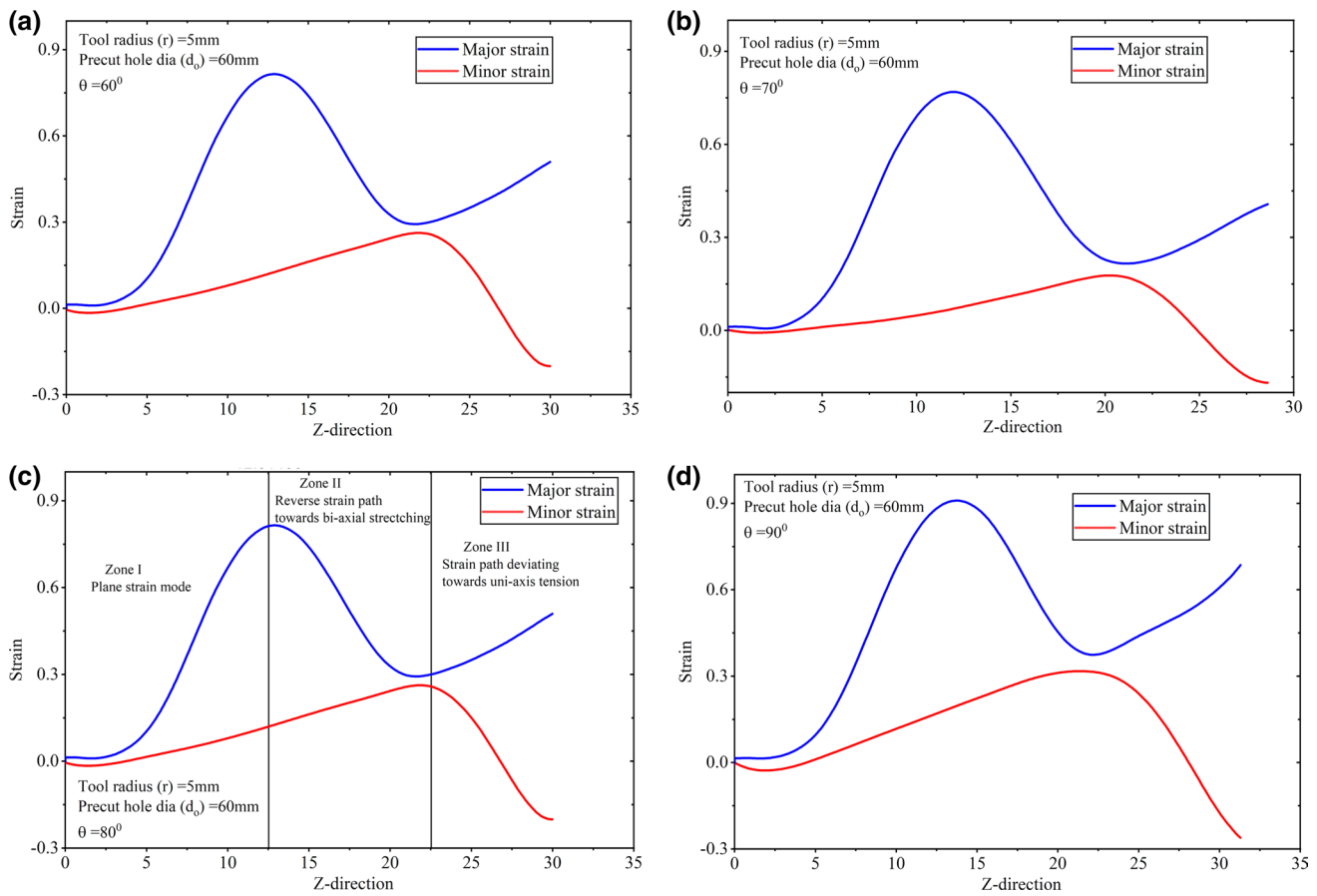
Fig. 12 Distribution of major and minor principal strains along with the flange depth

Table 5 Maximum percentage thickness reduction for all experimental conditions

Pre-cut hole diameter (mm)	1st stage (%)	2nd stage (%)	3rd stage (%)	4th stage
Ø45	45	55	66	–
Ø50	39	47	56	62
Ø60	27	33	41	46
Ø70	14	19	24	28

$\varepsilon_{1f} - 1.04\varepsilon_{2f} = 1.58$. Six different fracture models incorporating Hill48 anisotropy plastic theory were successfully calibrated. The Ayyada ductile damage model showed a very close fit to experimental FFLD throughout the strain ratio domain ranging from the uniaxial tension to balanced biaxial tension condition.

- The strain distribution pattern in the IHF deformed cup can be divided into three zones. Firstly, zone 1 referring to plane strain deformation mode, the major deformation occurred in the meridional direction and negligible strains in the circumferential direction. In zone 2, the major strain is decreasing, and minor strain is increasingly led to bi-axial tension deformation mode. Finally, zone 3, where the material is subjected to uni-axial tension in the circumferential direction towards the edge of the pre-cut hole.

- Experimental and Ayyada FFLD incorporating Hill48 plasticity theory was implemented as damage criteria in FE codes to predict the formability performance in the multi-stage IHF process. The predicted strain distributions, part depth, thickness distribution, and vertical force profile matched accurately with the experimental data within a 6% error for different pre-cut hole diameter and stages investigated.

- The force encountered in stage-1 increases to maximum value up to a certain depth of flange and then decreasing due to the presence of a hole at the center of the blank. The force is increasing with depth in all subsequent stages till the final depth due to sheet stretching. Further, the maximum force is decreasing with an increase in the number of stages due to the domination of thinning over the strain hardening. The maximum
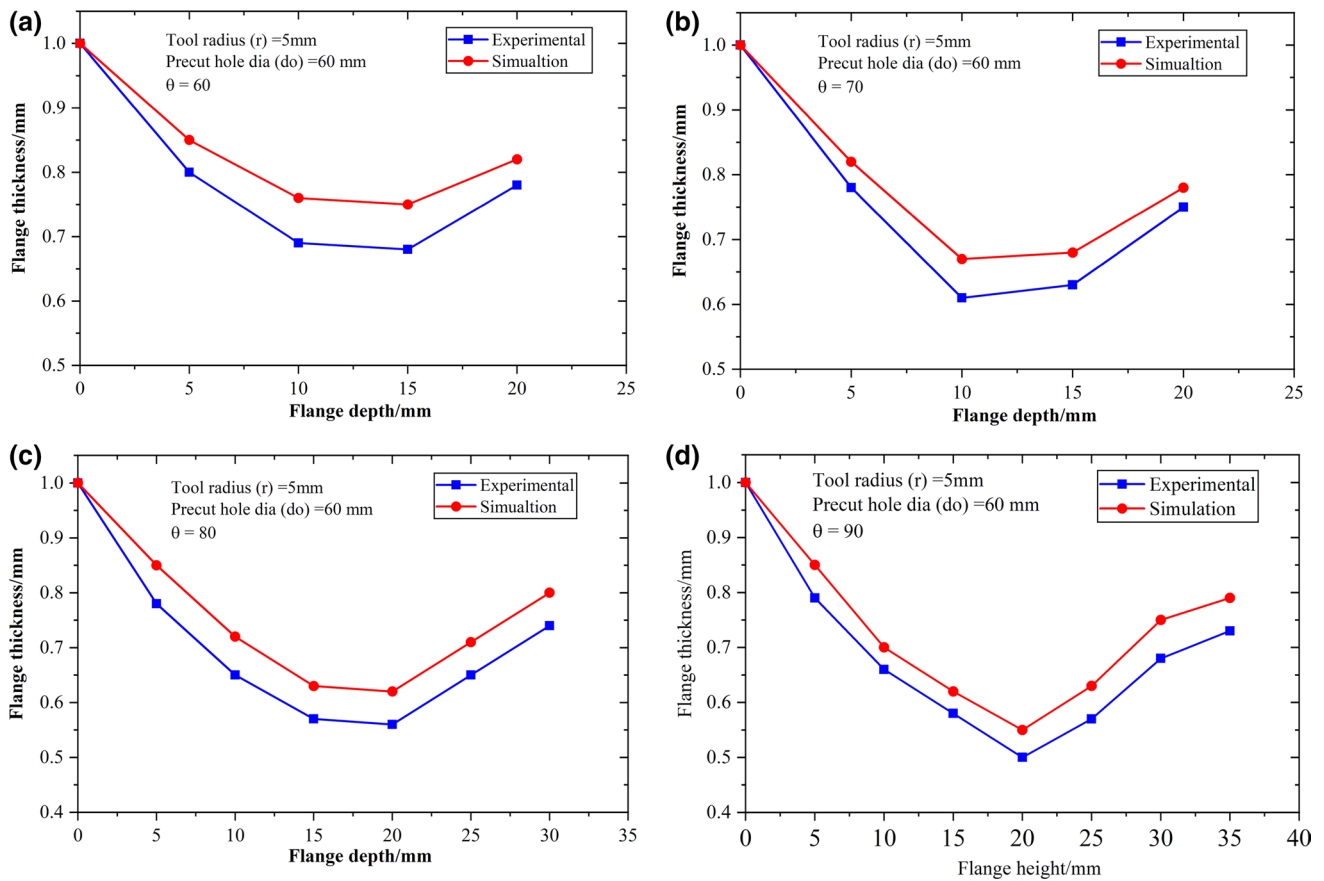
Fig. 13 Experimental and simulation thickness distribution for incremental hole flanging process with a 60 mm pre-cut hole diameter

force 1600 N observed in IHF is very negligible compared to the forming forces in CHF.

- The thickness distribution in IHF is like a trough shape. The thickness is decreasing up to a certain depth and then increasing towards the edge of the hole. The maximum thickness reduction was found to be 28%, 45% and 60% for parts with 70 mm, 60 mm and 50 mm precut hole diameters, respectively. The thickness reduction at the fracture in case 45 mm pre-cut hole diameter was found to be 66%.

- The surface roughness was found to decreases from 1.15 to 0.65 µm, with an increase in the number of stages. This improvement in surface quality was due to burnishing action between the tool and blank. Additionally, the effect of the pre-cut hole on surface roughness seems to be insignificant.
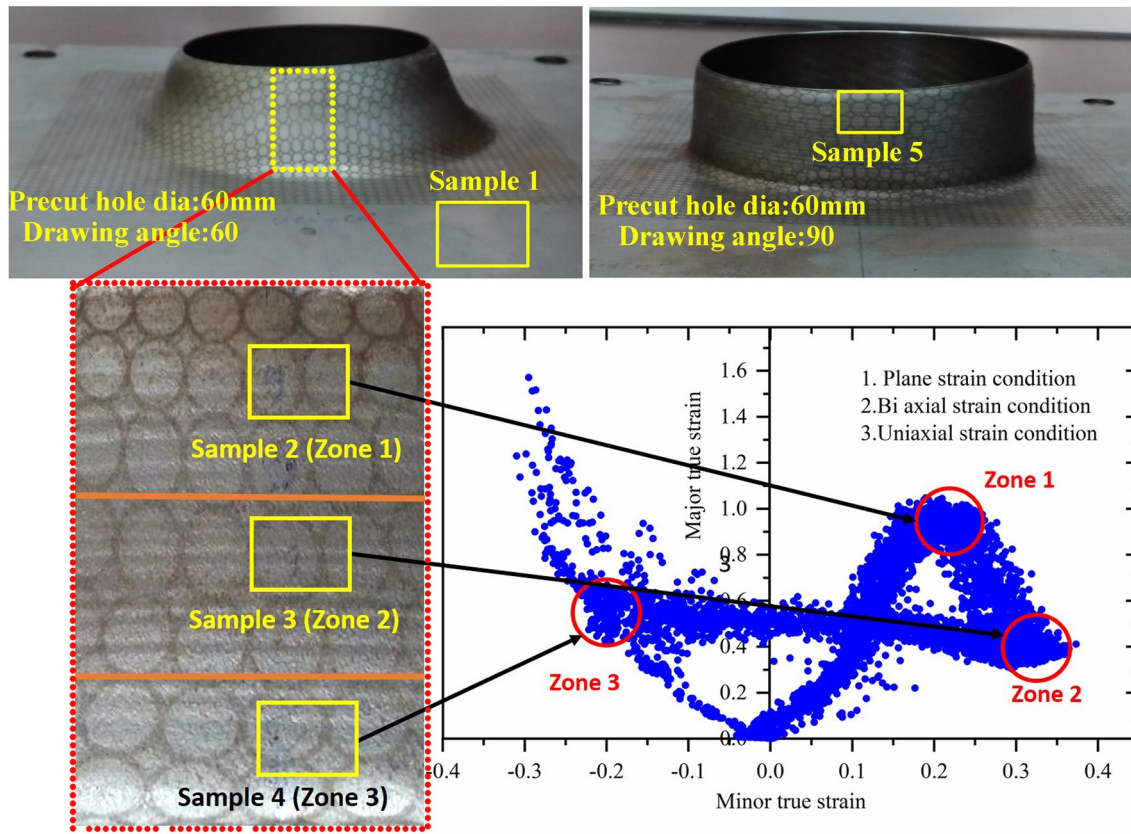
Fig. 14 Samples cut from the base material and different deformation zones for microtexture analyses
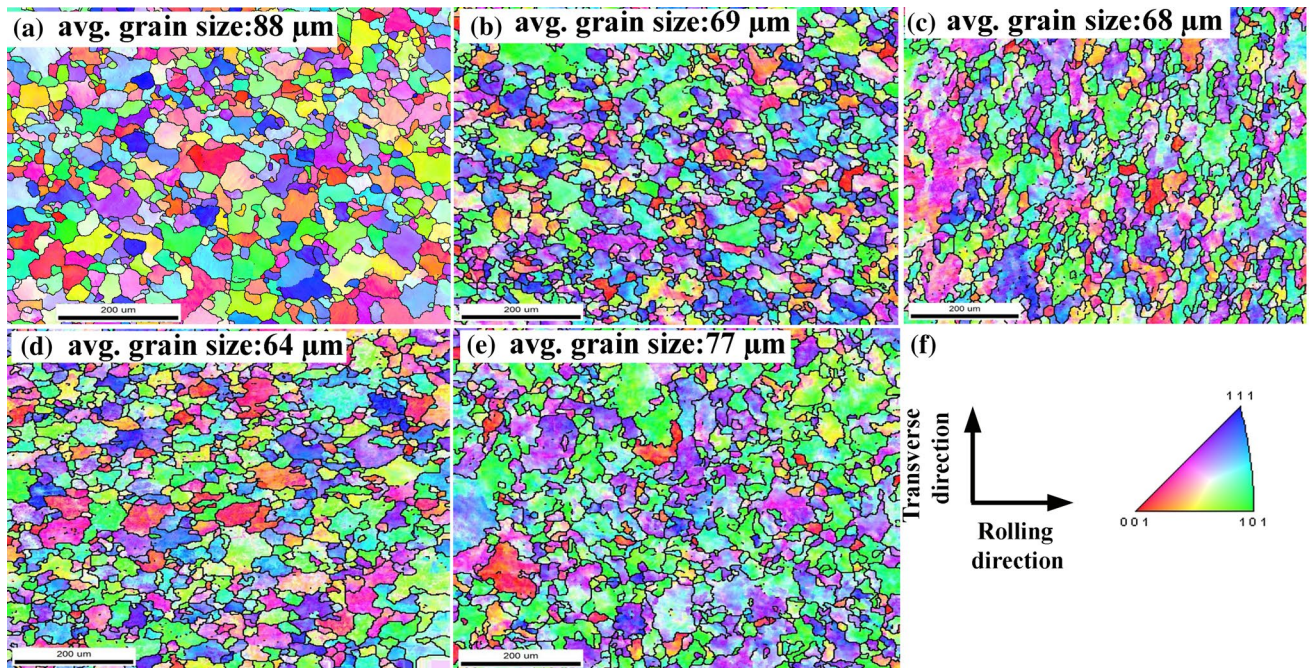

Fig. 15 Inverse pole figure (IPF) of **a** base material (sample 1), flanging angle of 60° at **b** zone 1 (sample 2), **c** zone 2 (sample 3), **d** zone 3 (sample 4), **e** flanging angle of 90° (sample 5), and **f** reference geometries
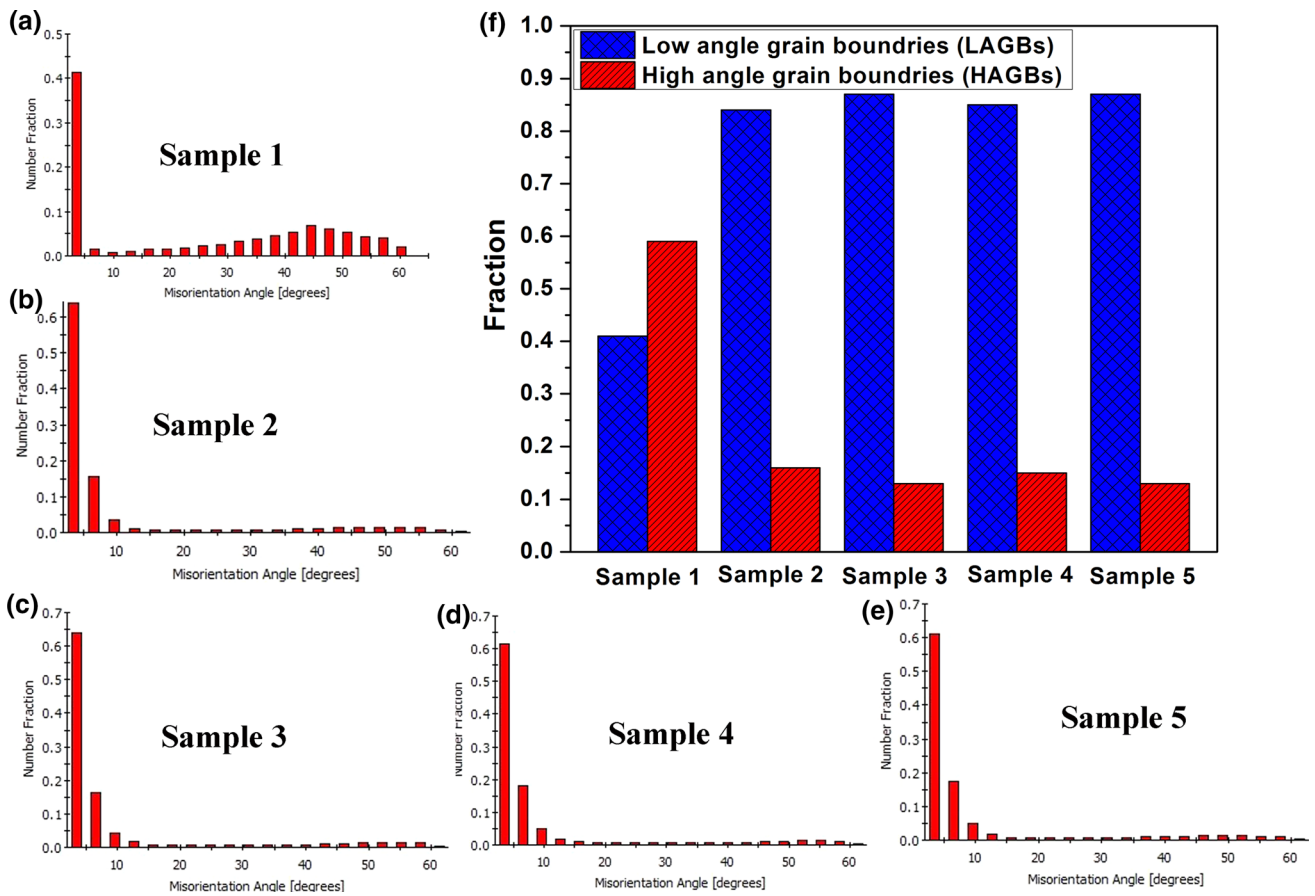
Fig. 16 Misorientation angle of **a** base material (sample 1), **b** zone 1 (sample 2), **c** sample 3, **d** sample 4, **e** sample 5, and **f** consolidated LAGBs and HAGBs fraction for all cases
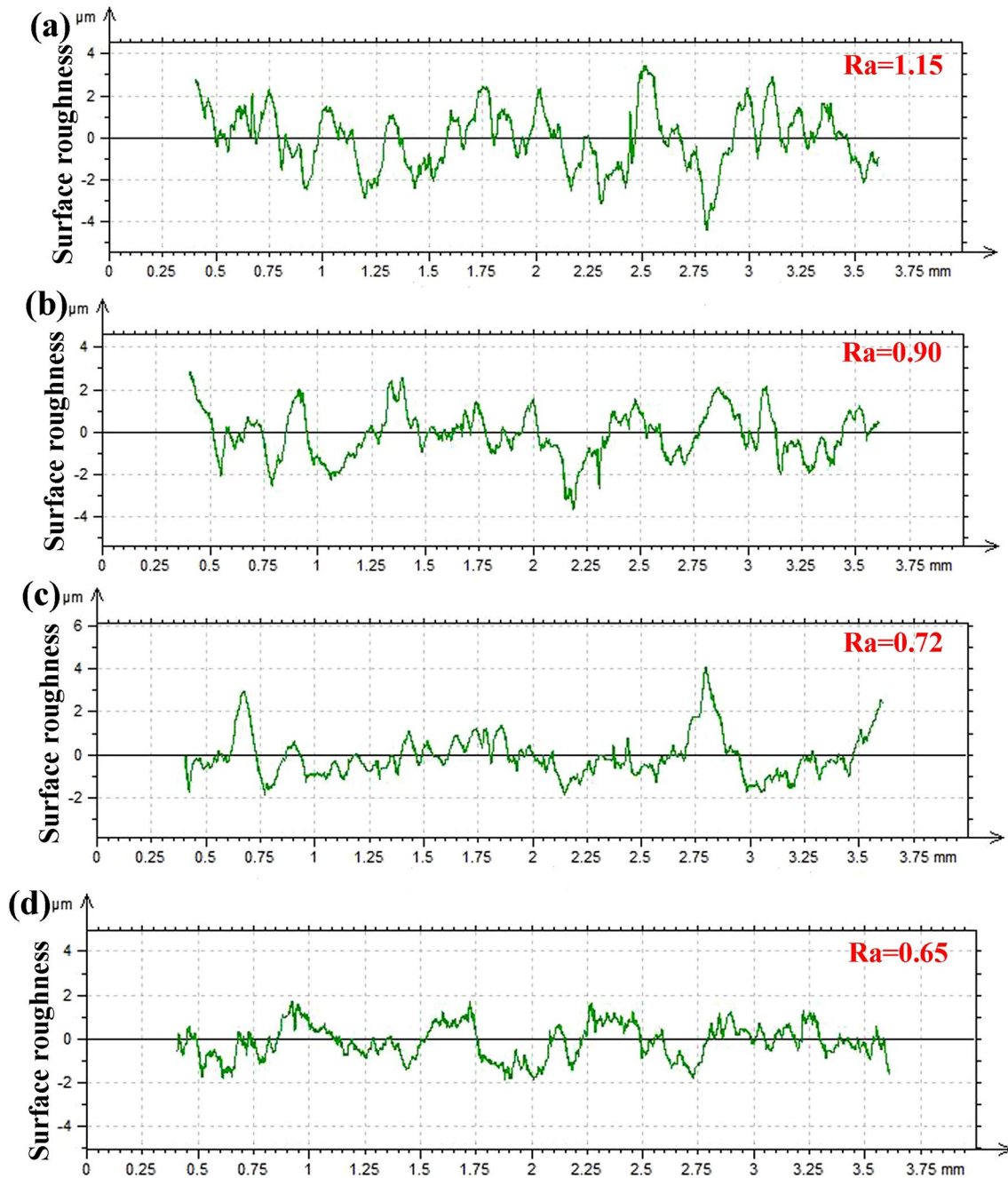
Fig. 17 Surface roughness profiles for 60 mm pre-cut hole diameter with flanging angle of **a** 60°, **b** 70°, **c** 80°, and **d** 90°

Compliance with ethical standards

Conflict of interest We confirm that there are no known conflicts of interest associated with this work.

Ethical standards The authors state that ethical standards were not violated when preparing the paper.

References

1. Kalpakjian S, Schmid SR. Manufacturing engineering and technology. 7th ed. Pearson; 2014

2. Dewang Y, Purohit R, Tenguria N. A study on sheet metal hole-flanging process. Mater Today Proc. 2017;4:5421–8.

3. Chen T-C. An analysis of forming limit in the elliptic hole-flanging process of sheet metal. J Mater Process Technol. 2007;192:373–80.

4. Huang J, Li S, Rao J, Zhang HM, Li XF. Study on process parameter optimization method by numerical simulation of sheet metal forming. J Chin Mech Eng. 2004;15:648–54.

5. Huang Y-M, Chien KH. Influence of cone semi-angle on the formability limitation of the hole-flanging process. Int J Adv Manuf Technol. 2002;19:597–606.

6. Thipprakmas S, Jin M, Murakawa M. Study on flanged shapes in fineblanked-hole flanging process (FB-hole flanging process) using finite element method (FEM). J Mater Process Technol. 2007;192:128–33.

7. Hyun DI, Oak SM, Kang SS, Moon YH. Estimation of hole flangeability for high strength steel plates. J Mater Process Technol. 2002;130:9–13.

8. Tang SC. Large elasto-plastic strain analysis of flanged hole forming. Comput Struct. 1981;13:363–70.

9. Krichen A, Kacem A, Hbaieb M. Blank-holding effect on the hole-flanging process of sheet aluminum alloy. J Mater Process Technol. 2011;211:619–26.

10. Stachowicz F. Estimation of hole-flange ability for deep drawing steel sheets. Arch Civ Mech Eng. 2008;8:167–72.

11. Huang Y-M, Chien K-H. The formability limitation of the hole-flanging process. J Mater Process Technol. 2001;117:43–51.

12. Takuda H, Mori K, Fujimoto H, Hatta N. Prediction of forming limit in bore-expanding of sheet metals using ductile fracture criterion. J Mater Process Technol. 1999;92:433–8.

13. Elbitar T, Gemeal A. Finite element analysis of deep drawing and hole flanging processing of an oil filter cover. Int J Mater Form. 2008;1:125–8.

14. Uthaisangsuk V, Prahl U, Bleck W. Stretch-flangeability characterisation of multiphase steel using a microstructure based failure modelling. Comput Mater Sci. 2009;45:617–23.

15. Comstock RJ, Scherrer DK, Adamczyk RD. Hole expansion in a variety of sheet steels. J Mater Eng Perform. 2006;15:675–83.

16. Adamczyk RD, Michal GM. Sheared edge extension of high-strength cold-rolled steels. J Appl Metalwork. 1986;4:157–63.

17. Su H, Huang L, Li J, Ma F, Ma H, Huang P, et al. Inhomogeneous deformation behaviors of oblique hole-flanging parts during electromagnetic forming. J Manuf Process. 2020;52:1–11.

18. Bansal A, Lingam R, Yadav SK, Reddy NV. Prediction of forming forces in single point incremental forming. J Manuf Process. 2017;28:486–93.

19. He A, Wang C, Liu S, Meehan PA. Switched model predictive path control of incremental sheet forming for parts with varying wall angles. J Manuf Process. 2020;53:342–55.

20. Raju C, Haloi N, Narayanan CS. Strain distribution and failure mode in single point incremental forming (SPIF) of multiple commercially pure aluminum sheets. J Manuf Process. 2017;30:328–35.

21. Min J, Kuhlenkötter B, Shu C, Störkle D, Thyssen L. Experimental and numerical investigation on incremental sheet forming with flexible die-support from metallic foam. J Manuf Process. 2018;31:605–12.

22. Raujol-Veillé J, Toussaint F, Tabourot L, Vautrot M, Balland P. Experimental and numerical investigation of a short, thin-walled steel tube incremental forming process. J Manuf Process. 2015;19:59–66.

23. Montanari L, Cristino VA, Silva MB, Martins PAF. A new approach for deformation history of material elements in hole-flanging produced by single point incremental forming. Int J Adv Manuf Technol. 2013;69:1175–83.

24. Cristino VA, Montanari L, Silva MB, Atkins AG, Martins PAF. Fracture in hole-flanging produced by single point incremental forming. Int J Mech Sci. 2014;83:146–54.

25. Cui Z, Gao L. Studies on hole-flanging process using multistage incremental forming. CIRP J Manuf Sci Technol. 2010;2:124–8.

26. Cao T, Lu B, Ou H, Long H, Chen J. Investigation on a new hole-flanging approach by incremental sheet forming through a featured tool. Int J Mach Tools Manuf. 2016;110:1–17.

27. Borrego M, Morales-Palma D, Martinez-Donaire AJ, Centeno G, Vallellano C. Experimental study of hole-flanging by single-stage incremental sheet forming. J Mater Process Technol. 2016;237:320–30.

28. ASTM E8/E8M-16ae1, Standard Test Methods for Tension Testing of Metallic Materials, ASTM International: West Conshohocken, PA; 2016. https://doi.org/10.1520/E0008_E0008M-16AE01(www.astm.org)

29. Prasad KS, Panda SK, Kar SK, Sen M, Murty SN, Sharma SC. Microstructures, forming limit and failure analyses of INCONEL 718 sheets for fabrication of aerospace components. J Mater Eng Perform. 2017;26:1513–30. https://doi.org/10.1007/s11665-017-2547-4.

30. Prasad KS, Panda SK, Kar SK, Singh SK, Murty SVSN, Sharma SC. Effect of temperature and deformation speed on formability of IN718 sheets: experimentation and modelling. IOP Conf Ser Mater Sci Eng. 2018. https://doi.org/10.1088/1757-899X/418/1/012055.

31. Elford M, Saha P, Seong D, Haque MDZ, Yoon JW. Benchmark 3-Incremental sheet forming. AIP Conf Proc. 2013;1567:227–61.

32. Surech K, Regalla SP. Effect of time scaling and mass scaling in numerical simulation of incremental forming. Appl Mech Mater. 2014;612:105–10.

33. Panicker SS, Prasad KS, Sawale G, Hazra S, Shollock B, Panda SK. Warm redrawing of AA6082 sheets and investigations into the effect of aging heat treatment on cup wall strength. Mater Sci Eng A. 2019;768:138445.

34. Basak S, Prasad KS, Mehto A, Bagchi J, Ganesh YS, Mohanty S, et al. Parameter optimization and texture evolution in single point incremental sheet forming process. Proc Inst Mech Eng Part B J Eng Manuf. 2019;234:126–39.

35. Singh SK, Limbadri K, Singh AK, Ram AM, Ravindran M, Krishna M, et al. Studies on texture and formability of Zircaloy-4 produced by pilgering route. J Mater Res Technol. 2019;8:2120–9.

36. Ko YK, Lee JS, Huh H, Kim HK, Park SH. Prediction of fracture in hub-hole expanding process using a new ductile fracture criterion. J Mater Process Technol. 2007;187–188:358–62.

37. Habibi N, Zarei-Hanzaki A, Abedi HR. An investigation into the fracture mechanisms of twinning-induced-plasticity steel sheets under various strain paths. J Mater Process Technol. 2015;224:102–16.

38. Prasad KS, Panda SK, Kar SK, Murty SVSN, Sharma SC. Prediction of fracture and deep drawing behavior of solution treated Inconel-718 sheets: numerical modeling and experimental validation. Mater Sci Eng A. 2018;733:393–407.

39. Cockcroft MG, Latham DJ. Ductility and the workability of Metals. J Inst Met. 1968;96:33–9.

40. Mcclintock FA. A criterion for ductile fracture by the growth of holes. J Appl Mech. 1968;363:363–71.

41. Ayada M. Central bursting in extrusion of inhomogeneous materials. In: Proc. 2nd Int. Conf. Technol. Plast. Stuttgart, 1987, vol. 1, 1987, p. 553–8.

42. Rice JR, Tracey DM. On the ductile enlargement of voids in triaxial stress fields. J Mech Phys Solids. 1969;17:201–17.

43. Brozzo P, Deluca B, Rendina R. A new method for the prediction of formability in metal sheets, sheet material forming and formability. Proc. Seventh Bienn. Conf. IDDRG, 1972.

44. Oh SI, Chen CC, Kobayashi S. Ductile fracture in axisymmetric extrusion and drawing-part 2: workability in extrusoin and drawing. J Eng Ind. 1979;101:36–44.

45. Basak S, Prasad KS, Sidpara AM, Panda SK. Single point incremental forming of AA6061 thin sheet: calibration of ductile fracture models incorporating anisotropy and post forming analyses. Int J Mater Form. 2019;12:623–42.

46. Isik K, Silva MB, Tekkaya AE, Martins PAF. Formability limits by fracture in sheet metal forming. J Mater Process Technol. 2014;214:1557–65.

47. Kurra S, Regalla SP. Experimental and numerical studies on formability of extra-deep drawing steel in incremental sheet metal forming. J Mater Res Technol. 2014;3:158–71.

48. Cristino VAM, Silva MB, Wong PK, Martins PAF. Determining the fracture forming limits in sheet metal forming: a technical note. J Strain Anal Eng Des. 2017;52:467–71.

49. Silva MB, Skjoedt M, Atkins AG, Bay N, Martins PAF. Single-point incremental forming and formability–failure diagrams. J Strain Anal Eng Des. 2008;43:15–35. https://doi.org/10.1243/03093247JSA340.

50. Leu D-K, Chen T-C, Huang Y-M. Influence of punch shapes on the collar-drawing process of sheet steel. J Mater Process Technol. 1999;88:134–46.

51. Masoumi M, Silva CC, Béreš M, Ladino DH, de Abreu HFG. Role of crystallographic texture on the improvement of hydrogen-induced crack resistance in API 5L X70 pipeline steel. Int J Hydrogen Energy. 2017;42:1318–26.

52. Prasad KS, Panda SK, Kar SK, Murty SVSN, Sharma SC. Effect of solution treatment on deep drawability of IN718 sheets: experimental analysis and metallurgical characterization. Mater Sci Eng A. 2018;727:97–112. https://doi.org/10.1016/j.msea.2018.04.110.

53. Masoumi M, Silva CC, de Abreu HFG. Effect of crystallographic orientations on the hydrogen-induced cracking resistance improvement of API 5L X70 pipeline steel under various thermomechanical processing. Corros Sci. 2016;111:121–31.

Publisher's Note Springer Nature remains neutral with regard to jurisdictional claims in published maps and institutional affiliations.